Multi-decadal analysis of high-resolution albedo changes induced by urbanization over contrasted Chinese cities based on Landsat data

Tianci Guo, Tao He, Shunlin Liang, Jean-Louis Roujean, Yuyu Zhou, Xin Huang

▶ **To cite this version:**

Tianci Guo, Tao He, Shunlin Liang, Jean-Louis Roujean, Yuyu Zhou, et al.. Multi-decadal analysis of high-resolution albedo changes induced by urbanization over contrasted Chinese cities based on Landsat data. Remote Sensing of Environment, 2022, 269, pp.112832. 10.1016/j.rse.2021.112832 . hal-03817831

HAL Id: hal-03817831
https://hal.science/hal-03817831v1

Submitted on 19 Oct 2022

HAL is a multi-disciplinary open access archive for the deposit and dissemination of scientific research documents, whether they are published or not. The documents may come from teaching and research institutions in France or abroad, or from public or private research centers.

L'archive ouverte pluridisciplinaire **HAL**, est destinée au dépôt et à la diffusion de documents scientifiques de niveau recherche, publiés ou non, émanant des établissements d'enseignement et de recherche français ou étrangers, des laboratoires publics ou privés.

Distributed under a Creative Commons Attribution - NonCommercial - NoDerivatives 4.0 International License

Remote Sensing of Environment 269 (2022) 112832

Contents lists available at ScienceDirect

Remote Sensing of Environment

journal homepage: www.elsevier.com/locate/rse

Multi-decadal analysis of high-resolution albedo changes induced by urbanization over contrasted Chinese cities based on Landsat data

Tianci Guo [a], Tao He [a,b,*], Shunlin Liang [c], Jean-Louis Roujean [d], Yuyu Zhou [e], Xin Huang [a,b]

[a] School of Remote Sensing and Information Engineering, Wuhan University, Wuhan, Hubei 430079, China
[b] State Key Laboratory of Information Engineering in Surveying, Mapping and Remote Sensing, Wuhan University, Wuhan, Hubei 430079, China
[c] Department of Geographical Sciences, University of Maryland, College Park, MD 20742, USA
[d] CESBIO - Centre d'Etudes Spatiales de la BIOsphère, CNES-CNRS-INRAE-IRD-UPS, 31401 Toulouse, France
[e] Department of Geological and Atmospheric Sciences, Iowa State University, Ames, IA 50011, USA

ARTICLE INFO

Editor: Marie Weiss

Keywords:
Urbanization
Remote sensing
Albedo
Land cover change
Landsat

ABSTRACT

Surface albedo is a key parameter in the surface energy balance and has been identified as a primary essential climate variable (ECV). Variations in surface albedo can be used as a diagnostic tool for local climate change. This is particularly true in urban areas, where the impacts of land cover conversion due to increasing anthropogenic demands can be examined using surface albedo changes. Most of the previous studies of albedo in cities have relied on coarse-resolution datasets with short time spans and have disregarded continuous monitoring. In addition, it is still unclear which urbanization processes are involved and what effects they have on surface albedo over long time periods. This study aimed to identify the contribution of increasing urbanization to the regional climate by analyzing spatial and temporal changes in surface albedo. Assigning albedo values to land cover types is useful for determining the level of transformation and their impacts in various Chinese cities that underwent specific evolutions between 1986 and 2018. The Direct Estimation (DE) approach was modified to estimate the daily mean surface albedo at 30 m based on Landsat observations. It resulted root-mean-square errors (RMSEs) of less than 0.044 and bias about 0.006 between observations and model estimations. Such accuracy obtained after correcting the orbital drift of the Landsat satellite, was deemed satisfactory for detecting potential changes in albedo. Major findings are: 1) A notable trend was found over the past 33 years of 11 major Chinese cities, i.e. population about 10 million and more, with a general albedo increase from satellite observations. The higher resolution Landsat dataset showed a trend 3 times larger than the Global Land Surface Satellites (GLASS) product, which outlines the need for analyzing high resolution imagery in priority for reliable estimate of albedo over heterogeneous urban landscapes. 2) An increase in albedo infers a negative radiative forcing at an average rate of -2.771 W/m^2 per decade, thereby indicating a cooling effect for most Chinese cities. 3) Changes in surface albedo were also closely linked to landscape transformation, clearly observed using the 30 m resolution of the Landsat data. 4) Throughout the study period, surface albedo exhibited a temporal U-shaped curve in built-up areas under development, with albedo peaks in old and newly built districts and a decrease in albedo between the two eras.

1. Introduction

Urban areas represented only 3% of Earth's land surfaces in 2010 (Liu et al., 2014b); however, they have expanded rapidly in the past 20 years (Zhou et al., 2018b) and now host more than half of the total population of the Earth. The United Nations World Urbanization Prospects (WUP) has projected that, with ongoing rapid urbanization, the proportion of people living in urban areas will increase from 55% (2018 estimate) to 68% in 2050 foresight. Recent studies have confirmed a trend towards unprecedented global urbanization (Li et al., 2019; Liu et al., 2019; Radwan et al., 2019), and this process is likely to continue for decades (Bagan and Yamagata, 2014; Seto et al., 2014; Seto et al., 2012).

Urbanization contributes to global climate change in twofold: biogeochemically first as it increases carbon emissions because of additional people, consumption, and activation (Ali et al., 2019; Friedlingstein et al., 2019; Hong et al., 2019; Martínez-Zarzoso and

* Corresponding author.
E-mail address: taohers@whu.edu.cn (T. He).

https://doi.org/10.1016/j.rse.2021.112832
Received 22 November 2020; Received in revised form 23 October 2021; Accepted 26 November 2021
Available online 15 December 2021
0034-4257/© 2021 The Authors. Published by Elsevier Inc. This is an open access article under the CC BY-NC-ND license (http://creativecommons.org/licenses/by-nc-nd/4.0/).

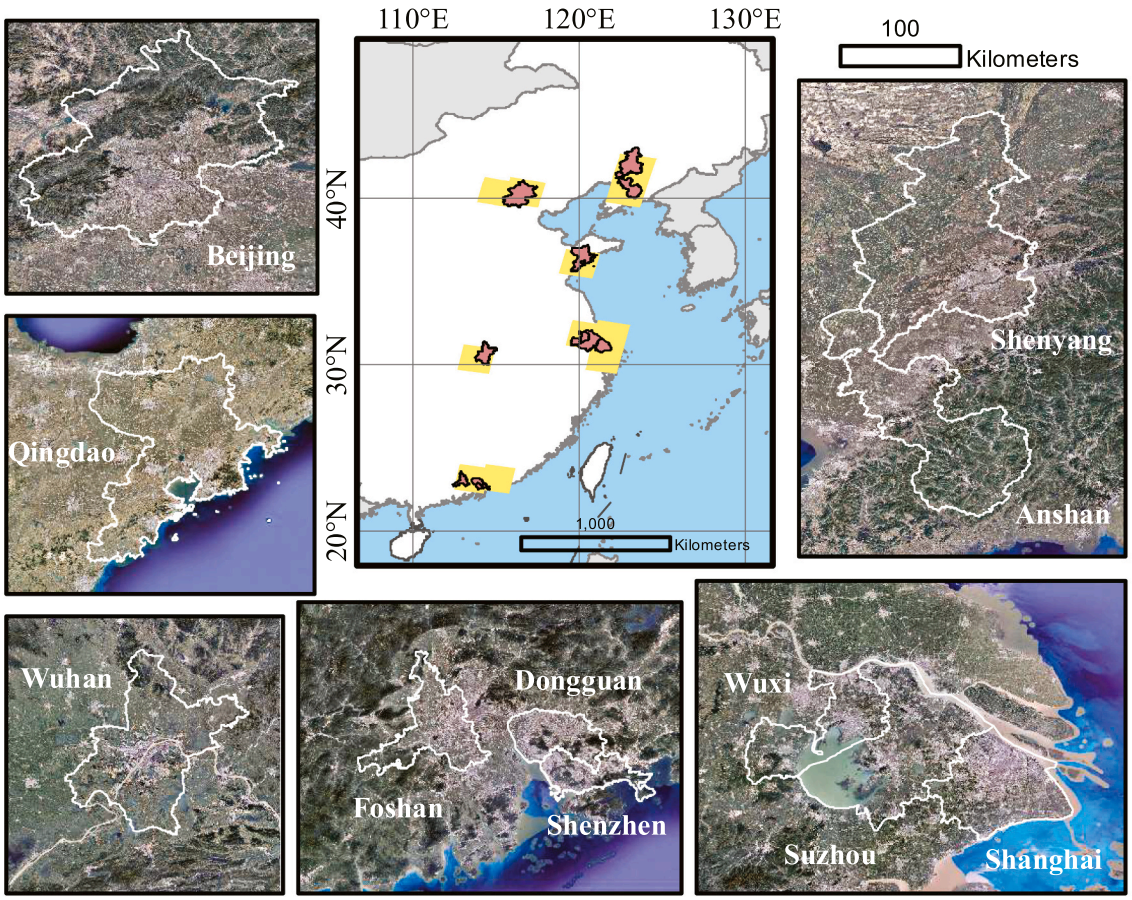

Fig. 1. Geographic location of the selected Chinese cities. The white boundaries are the administrative borders of the cities.

Maruotti, 2011); and secondly as it affects radiative forcing due to a modification of the geometry and the composition of surface elements (Kuang et al., 2019; McCarthy et al., 2010; Vahmani et al., 2016). The latter effect has a serious impact on local and regional climate due to alteration of the effective surface albedo (the ratio of the shortwave upward radiation from the surface to the shortwave downward radiation from the Sun) (Trlica et al., 2017), which leads to local phenomena such as urban heat islands (UHIs) (Chapman et al., 2019; Feng et al., 2019; Li and Zha, 2019; Li et al., 2017; Yao et al., 2017; Zhang and Liang, 2018; Zhou et al., 2018a).

Changes in surface albedo related to large-scale urban expansion will likely affect the climate of a region surrounding a large metropolitan area, due to an increased population density, with increased consumption and transportation (Barnes and Roy, 2010). Changes in albedo as a result of urbanization may constitute an important part of local and global climate forcing (Trlica et al., 2017). Therefore, the potential to offset UHI temperature effects through albedo manipulation (e.g. by using more reflective materials on rooftops) has become a topic of extensive discussion and concentrated research efforts using numerical simulations (Georgescu et al., 2014; Georgescu et al., 2013; Qin, 2015; Santamouris et al., 2011; Trlica et al., 2017). It has been reported that adopting highly and retro-reflective materials on urban surfaces (e.g., rooftops and pavement) can increase the net albedo in urban areas by ~0.01–0.1 (Akbari et al., 2012; Akbari et al., 2009; Mackey et al., 2012), as a consequence of a negative radiative forcing that causes a daytime cooling effect of ~0.7 K (Alchapar and Correa, 2016; Zhao et al., 2014). Studies have also established that a 0.1 increase in surface albedo in urban locations could lead to a long-term global cooling effect equivalent to counterbalancing ~25–150 billion tons of CO_2 emissions (Akbari et al., 2012; Tang et al., 2018). Several studies have combined radiometer data and remote sensing images to assess the albedos of various artificial materials in order to improve urban climate modeling (Ban-Weiss et al., 2015; Hamoodi et al., 2019; Shi et al., 2019).

Urbanization leads to albedo changes by altering natural vegetation or bare ground to manmade materials, including the complex topography effect, symbolized by an 'urban canyon' in built-up areas (Kuang et al., 2019; Santamouris et al., 2011; Tang et al., 2018; Trlica et al., 2017). Nevertheless, the effect of urbanization on albedo may lead to contrasting issues. While a bright material enhances the magnitude of the reflectivity, increasing the building density traps more radiation, thereby reducing the intensity of the total albedo.

Satellite albedo products have been used to assess the relationship between radiation effects and urban land changes (Cai et al., 2016), focusing on the expansion of impervious zones at the expense of green zones. Some studies have reported that urbanization can cause the albedo to increase (more solar radiation is reflected by Earth's surface) due to the introduction of light building materials (Feng et al., 2012; Kuang et al., 2019) and less vegetation cover (Hou et al., 2014). Other studies have suggested that urbanization has led to a decline in the urban surface albedo due to dark streets, building facades, and roofs that have replaced vegetated attributes with urban elements (Jacobson et al., 2015; Trlica et al., 2017). Such varied responses could be explained by an examination of the situation at different stages of urban development, which was dependent on the heterogeneity among the cities.

Studies of urban canyons have demonstrated that albedo measurements are heavily dependent on the structure (building density and height distribution) (Qin, 2015; Santamouris et al., 2011; Yang and Li, 2015). Hu et al. (2019) found that after rapid urbanization, settlements or urban surface structures became more complex, with higher buildings and enhanced radiation trapping. Both positive and negative urban-

Table 1
The selected representative 11 cities.

City level	Population (million)	City names
Level 1	>10	Shanghai, Beijing, Shenzhen, Suzhou, Wuhan
Level 2	8– 10	Qingdao, Shenyang, Dongguan
Level 3	<8	Foshan, Wuxi, Anshan

Table 2
Landsat Path/Row of study area.

City Name	Path/Row	
Shanghai	118/038	118/039
Beijing	123/032	
Shenzhen	122/044	121/044
Suzhou	119/038	
Wuhan	123/039	
Qingdao	120/035	
Shenyang	119/031	
Dongguan	122/044	
Foshan	122/044	
Wuxi	119/038	
Anshan	119/032	

rural differences have been reported in single cities (Manoli et al., 2019). Sugawara and Takamura (2014) analyzed airborne data over cities and found that the albedo was lower in areas with more buildings, and decreased as the aspect ratio of street canyons increased. From numerical simulations, Yang and Li (2015) illustrated that the average urban albedo was the lowest in a medium-density city with high-rise buildings that had larger building height differences.

Previous studies of remotely sensed urban albedo have mostly considered coarse-resolution data such as from the Moderate Resolution Imaging Spectroradiometer (MODIS) with a 500 m resolution (Jun et al., 2013; Reinmann et al., 2016; Wang et al., 2006; Zoran et al., 2018), or the Global Land Surface Satellites (GLASS) shortwave surface albedo product (Hu et al., 2019; Hu et al., 2016; Tang et al., 2018). Several urban remote sensing studies have determined that changes in urban landscapes usually occur on small scales (Jin et al., 2005; Trlica et al., 2017; Zhou et al., 2014). However, the lack of high-resolution urban albedo data has limited in-depth explorations of the causes of changes in various urban functional zones (Feng et al., 2019). Studies using satellite imagery to analyze temporal changes in urban albedo have mostly used the 'endpoints' approach (Woodcock et al., 2020), which relies on the difference in albedo between the initial year and the final years of the study period (Feng et al., 2012; Kuang et al., 2019; Royer et al., 1988). The outcomes may be questionable because additional changes in albedo could occur in the middle of the time series, which is a feature that has rarely been explored.

The use of Landsat Thematic Mapper (TM) images as a data source requires the consideration of orbital drift. The Landsat 5 orbit was relatively stable during the periods of 1984–1994 and 2007–2011, but the periods of 1995–2000 and 2003–2007 had significant deviations in satellite positioning (Gao et al., 2014; Zhang and Roy, 2016). It has been reported that the difference in nadir reflectance between Landsat 5 TM overpass times and a fixed 10 a.m. local time can reach 0.015 and 0.018 for the red and NIR bands, respectively (Gao et al., 2014). The overpass time of the TM has been continuously delayed, which has produced an unrealistic decrease in the observed albedo during the lifetime of the satellite. This has previously been disregarded in analyses of the Landsat TM data that focused on albedo time series (Feng et al., 2012; Hou et al., 2014; Hu et al., 2016; Kuang et al., 2019).

As the largest developing country, China has experienced rapid urbanization and economic development (Liu et al., 2019), with the urban population soaring from 25% in the 1980s to 60% in 2018 (Gong et al., 2012; Guan et al., 2018). Due to increasing human activity, carbon emissions from cities account for 85% of the total in China (Shan et al., 2018), which directly contributes to global warming. As China's cities have undergone different stages of urbanization, the associated surface albedo changes may have been complex. This study may be helpful for understanding the historical background of changes in the surface energy budget, as well as for future decisions that foster the urban development.

The main goal of this study is to understand the changes in surface albedo during the summer in 11 Chinese cities characterized by rapid urbanization, and to develop a method for estimating the daily average surface albedo. The study was conducted over a long period (1986–2018) by analyzing Landsat data (30 m resolution). We also discussed how land cover changes affected patterns of changes in albedo, and how they modified the radiative forcing in the study area.

2. Materials and method

2.1. Study area

In this study, we selected 11 cities (Fig. 1) at different stages of economic development and urbanization to study the impact of growing cities on albedo and surface radiative forcing. Three characteristics were considered when selecting the cities: population, gross domestic product (GDP), and location (Huang et al., 2019). China's first wave of urbanization occurred in coastal areas, from which 7 representative cities were selected, forming three mega-urban agglomerations (Lyu et al., 2018; Schneider and Mertes, 2014): the Yangtze River Delta (Shanghai, Wuxi, and Suzhou), Pearl River Delta (Shenzhen, Foshan, and Dongguan), and the Beijing-Tianjin-Hebei region (Beijing). Considering that China's early industrialization began in the northeastern part of the country, two cities from that region (Shenyang and Anshan) were also selected. Wuhan was chosen to represent the cities in central China. In addition, Qingdao was selected to represent northern Chinese urban agglomerations. Furthermore, in order to determine the changes in albedo in cities with different economic volumes and populations, we classified the 11 cities into three categories (Table 1) based on their 2015 populations (Güneralp et al., 2020; Huang et al., 2019).

2.2. Data sources

2.2.1. Landsat data

The Landsat program is the longest-running enterprise for the acquisition of satellite imagery of the Earth system. In the absence of other types of monitoring, Landsat remains the best data source for estimating any changes in surface albedo effects at fine-scale resolution on a continental scale (Markham and Helder, 2012). However, radiometric calibration control is necessary for sensors onboard the Landsat satellites. Such efforts have been conducted regularly throughout the last three decades to calibrate the system with an absolute accuracy of 5% (Chander et al., 2009; Markham et al., 2014), as well as good temporal consistency (Kim et al., 2013). Level 1 T (L1T) data is the highest quality product in level 1 for time series analysis, with a geolocation uncertainty of less than a half pixel for Thematic Mapper (TM), Enhanced Thematic Mapper Plus (ETM+), and Operational Land Imager (OLI) images (He et al., 2018). Such accuracy relies on terrain correction, which provides the necessary radiometric and geodetic accuracy by incorporating ground control points, while using a digital elevation model (DEM) for topographic displacements (Chander et al., 2004; Chander and Markham, 2003; Kim et al., 2013; Roy et al., 2014).

Landsat TM images from 1986 to 2011 and Landsat OLI images from 2013 to 2018 during the summer (June, July, and August) were used to estimate the surface albedo. Only data acquired in clear sky conditions or that had effective cloud removals using the Function of Mask (Fmask) version 4 (Qiu et al., 2019) were considered in this study. Table 2 represents the Landsat Path/Row values corresponding to the study area and, Fig. 2 shows the number of scenarios used per year.

The Landsat Surface Reflectance product (Collection 1 Level 2)

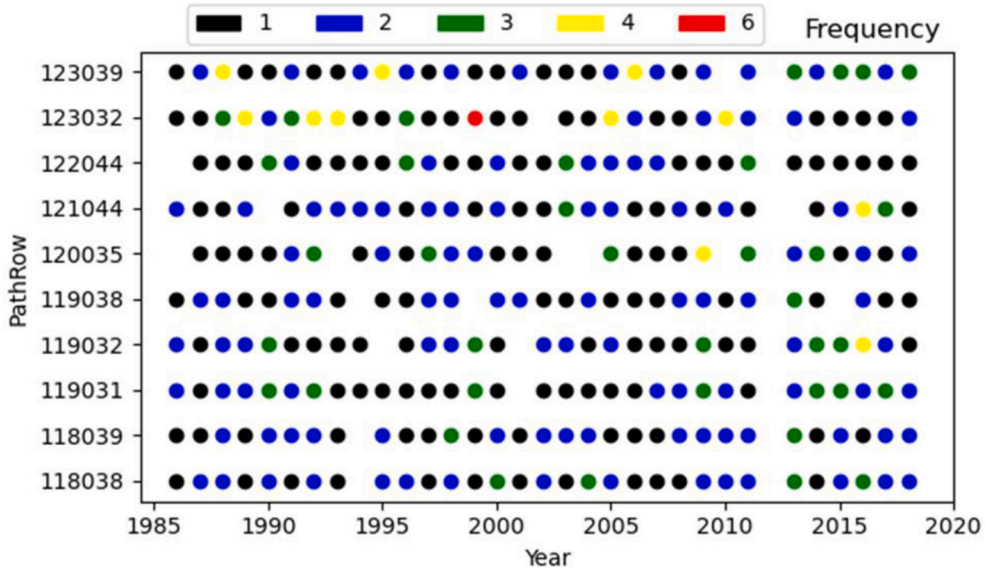

Fig. 2. The frequency of each path/row of Landsat images used in each year.

Table 3
List of information of the ground stations used in this study.

Site name	Landsat Path/Row	Network	Center Latitude/Longitude (°N/°E)		Land cover	Tower height (m)
BON	023/032	SURFRAD	40.05° N	88.37° W	Cropland	10
TBL	034/032	SURFRAD	40.12° N	105.24° W	Grassland	10
DRA	040/035	SURFRAD	36.62° N	116.02° W	Open shrub land	10
FPK	035/026	SURFRAD	48.31° N	105.10° W	Grassland	10
GWN	023/036	SURFRAD	34.25° N	89.87° W	Grassland	10
PSU	016/032	SURFRAD	40.72° N	77.93° W	Cropland	10
SXF	029/030	SURFRAD	43.73° N	96.62° W	Grassland	10
Yakou	133/034	Heihe	38.01° N	100.24° E	Alpine meadow	6
Zhangye	133/033	Heihe	38.98° N	100.45° E	Reed	6
Huazhaizi	133/033	Heihe	38.77° N	100.32° E	Desert	6
Arou	133/034	Heihe	38.05° N	100.46° E	Subalpine meadow	5
Daman	133/033	Heihe	38.86° N	100.37° E	Maize	12
Dashalong	134/033	Heihe	38.84° N	98.94° E	Marsh alpine meadow	6
Ebao	133/034	Heihe	37.95° N	100.92° E	Alpine meadow	6
Heihe	133/033	Heihe	38.83° N	100.48° E	Grassland	1.5
Desert	134/031	Heihe	42.11° N	100.99° E	Reaumuria desert	6
MixedForest	133/031	Heihe	41.99° N	101.13° E	Populus euphratica and Tamarix	24
Jingyangling	133/034	Heihe	37.84° N	101.12° E	Alpine meadow	6
Sidaoqiao	133/031	Heihe	42.00° N	101.14° E	Tamarix	10

(Masek et al., 2006; Vermote et al., 2016) for the same periods was used to obtain the normalized difference vegetation index (NDVI) throughout the study area (Shanghai, Foshan, and Suzhou). Processing of the Landsat Surface Reflectance dataset includes the elimination of atmospheric effects to reach a steady uncertainty over time (Claverie et al., 2015; Vermote et al., 2016). These data are available from the Earth Explorer (https://earthexplorer.usgs.gov/) program developed by the United States Geological Survey (USGS).

2.2.2. GLASS albedo products

The Global Land Surface Satellite (GLASS) project (http://glass-product.bnu.edu.cn/) aims to provide a suite of important land surface parameter datasets with high temporal resolution and accuracy for global change studies (Liu et al., 2013a). It provides long-term global surface broadband albedo product from 1981 to 2010, which is a combination of Advanced Very High Resolution Radiometer (AVHRR, 1981–1999) and MODIS (2000−2010) data (Liang et al., 2013) with an accuracy similar to that of the broadly used MODIS MCD43 product (Liu et al., 2013b). The GLASS albedo product is a gap-filled dataset with long-term continuity and self-consistency (Liu et al., 2013b; Qu et al., 2014). In this study, the 0.05-degree resolution GLASS albedo product was used and compared with the Landsat albedo data to help assess the effects of spatial resolution on long-term albedo trend analysis.

2.2.3. Ground measurements

Accessing precise ground-based measurements in different climatic regions is essential for refining and verifying satellite-based estimates. In this study, in-situ data from the Surface Radiation budget (SURFRAD) network and the Heihe Integrated Observatory Network (Table 3) were used for validation.

The SURFRAD network was established in 1993 by the National Oceanic and Atmospheric Administration (NOAA) Office of Global Programs (Augustine et al., 2000; Augustine et al., 2005) and consists of seven stations. Ground measurements of surface albedo were calculated as the ratio of total upward to total downward radiation, or the blue-sky albedo, which is a useful variable for radiation budget assessments. SURFRAD datasets are freely available (ftp://aftp.cmdl.noaa.gov/data/radiation/surfrad/RadFlux/).

The method used for Landsat albedo estimation in this study has been extensively evaluated at globally distributed sites (He et al., 2018); however, previous validation efforts have rarely included sites in China. The Heihe integrated observatory network was established in 2007

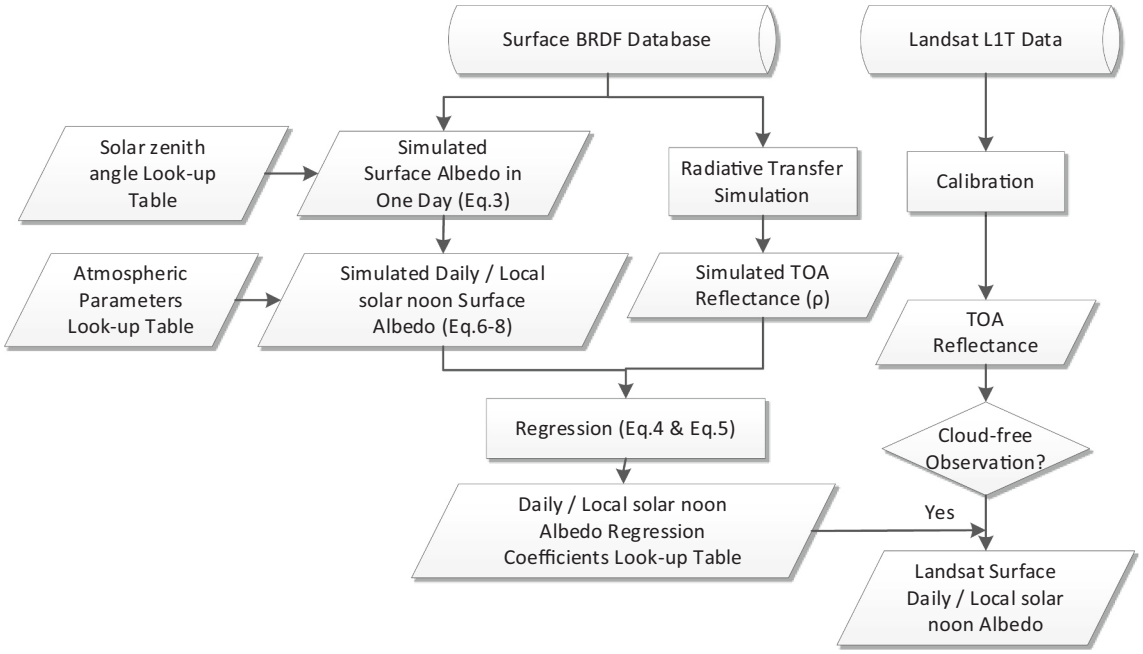

Fig. 3. Flowchart of local solar noon and daily albedo estimation from Landsat data.

Table 4
Configurations of LUT for simulating surface albedo and TOA reflectance data.

Parameters	Value
Solar zenith angle (°)	0, 20, 40, 60, and 70
View zenith angle (°)	0 and 15
Relative azimuth angle (°)	0, 30, 60, 90, 120, 150, and 180
Aerosol optical depth at 555 nm	0.05, 0.10, 0.15, 0.20, 0.30, 0.40, and 0.60
Latitude (°)	0, 10, 20, 30, 40, 50, and 60
Day of year	1, 32, 63, 94, 125, 156, 187, 218, 249, 280, 311, 342

during the Heihe Watershed Allied Telemetry Experimental Research (WATER) experiment and was completed in 2013 during the Heihe Watershed Allied Telemetry Experimental Research (HiWATER) experiment (Liu et al., 2018). The surface fluxes and meteorological parameters were derived from superstations and ordinary stations (including up to 23 observation stations) encompassing the entire Heihe River Basin (HRB). These data are also freely available (http://heihe.westgis.ac.cn/).

2.2.4. Land cover datasets

Land-use/land-cover (LUCC) data (Liu et al., 2014a; Liu et al., 2002) was obtained from the Data Center for Resources and Environmental Sciences at the Chinese Academy of Sciences (RESDC) (http://www.resdc.cn). We used seven epochs (late 1980, 1990, 1995, 2000, 2005, 2010 and 2015) of the data, all of which had 100 m spatial resolutions. The main data sources of the LUCC database are the Landsat Multispectral Scanner (MSS), TM, and ETM+, supplemented by data from the China-Brazil Earth Resource Satellite (CBERS). The LUCC database was generated from visual interpretations of remote sensing images. The classification system of LUCC is divided into cropland, forests, grassland, water, built-up land and other unused land (Xu et al., 2012). This dataset has been widely used to study land use and land cover changes in China (Huang et al., 2019). The classification accuracy of the first level is better than 94.3% (Liu et al., 2014a).

2.2.5. Surface downward solar radiation data

Downward shortwave radiation (DSR) represents the incident solar radiation over the land surface in the shortwave spectrum (0.3–4 μm) and is the major energy source over the land surface. MCD18A1 (Collection 6.0) refers to the Level-3 (L3) Terra and Aqua combined MODIS-derived DSR product (Wang et al., 2020). MCD18A1 provides 3-h global data at 5 km resolution in a sinusoidal gridded map projection every day, and fills a long-persisting gap in the requirements of terrestrial modeling and application communities. Validation of MCD18A1 products using ground measurements has suggested that the MODIS land surface radiation products are reliable and highly accurate, with an average coefficient of determination of 0.91, a root mean square error (RMSE) of 90 W/m^2, and a bias of 17 W/m^2 (Liang and Wang, 2017).

2.3. Methods

2.3.1. Surface albedo estimation

Albedo estimation relies on an algorithm that is based on the Direct Estimation (DE) method, originally proposed by Liang et al. (1999), which is a unified, simple, and fast empirical algorithm. Unlike existing algorithms for Landsat albedo estimation (Shuai et al., 2011; Shuai et al., 2014; Wang et al., 2016; Wang et al., 2017), the DE method neither requires surface reflectance from an explicit atmospheric correction, nor requires concurrent clear-sky observations from the MODIS for bidirectional reflectance distribution function (BRDF) correction (instead relying on a pre-built BRDF database derived from MODIS products, which will be explained later). The DE algorithm has been applied to data from a variety of sensors, including MODIS (Liang, 2003), Visible Infrared Imaging Radiometer Suite (VIIRS) (Wang et al., 2013), Multi-angle Imaging SpectroRadiometer (MISR) (He et al., 2017), and Landsat (He et al., 2018).

The DE method consists of two steps (Liang, 2003; Liang et al., 2005). The first step simulates the top of atmosphere (TOA) directional reflectance and surface albedo under different surface and atmospheric conditions from a radiative transfer model. The second step develops empirical relationships between the simulated TOA reflectance and shortwave surface albedo in considering all simulations:

$$\alpha_{ins} = \sum \rho_i^{TOA} \cdot c_i + c_0 \quad (1)$$

where α_{ins} is the instantaneous surface albedo for the wavelength region

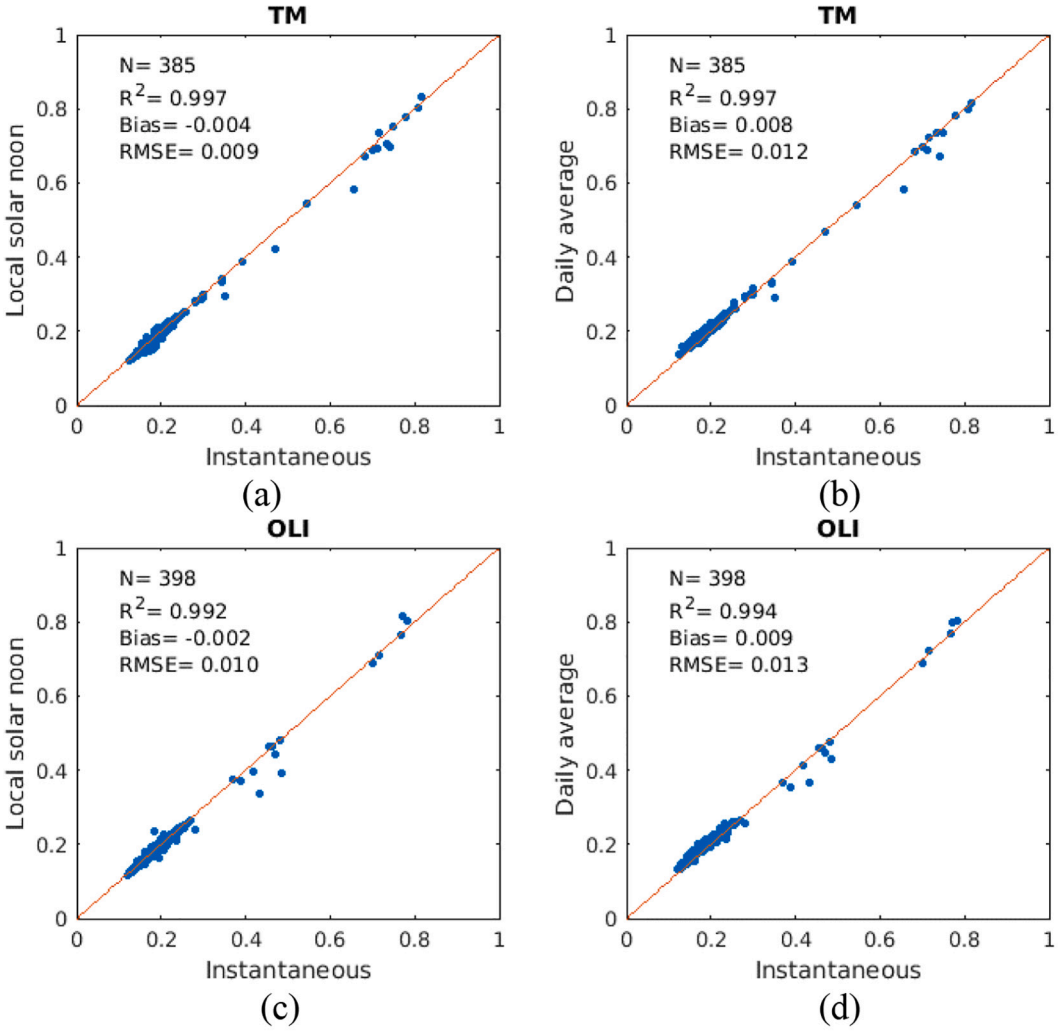

Fig. 4. Relationship between instantaneous and local solar noon albedo/daily albedo.

of 300-3000 nm; ρ_i^{TOA} is the TOA reflectance for the spectral band i; and c_i and c_0 are regression coefficients.

In earlier versions of the DE method, a spectral library was needed for surface albedo calculation as well as for TOA reflectance simulations. In addition, atmospheric parameters and sensor spectral responses were needed in TOA reflectance simulations (Liang, 2003; Liang et al., 2005; Liang et al., 1999).

To consider the surface anisotropic effects on both the surface albedo and TOA reflectance, a BRDF database was introduced to replace the surface reflectance spectral library for simulating the surface albedo and TOA reflectance (Wang et al., 2013). The BRDF database was built from the multiyear 500 m MODIS albedo products (MCD43A Collection 5) that consists of high-quality samples over different land cover types. Details of the BRDF database establishment refer to Wang et al. (2013) and He et al. (2018). The incorporation of surface BRDF improves the accuracy and stability of surface albedo estimates, especially for surface areas with strong anisotropy characteristics. Recently, such DE method has been further adapted and applied to Landsat data (He et al., 2018). The instantaneous Landsat albedo estimates have been validated extensively, and the data accuracy has been reported to have an RMSE of 0.022–0.034, with a long-term albedo stability difference of less than 0.003 (He et al., 2018). The empirical relationships between TOA reflectance and surface albedo were established on an angular-bin basis to reduce non-linear errors, as shown in Eq. (2).

$$\alpha_{ins} = \sum \rho_i^{TOA}(\theta_s, \theta_v, \varphi) \cdot c_i + c_0 \tag{2}$$

where α_{ins} is the instantaneous surface albedo for the wavelength region of 300-3000 nm; $\rho_i^{TOA}(\theta_s, \theta_v, \varphi)$ is the TOA reflectance with a solar zenith angle θ_s, view zenith angle θ_v, and relative azimuth angle φ for spectral band i; and c_i and c_0 are the regression coefficients.

Specifically, surface albedo, which is used to derive the statistical relationship in Eq. (1), can be calculated using the angular and spectral integrations of surface directional reflectance, with the support of surface BRDF kernel parameters, as shown in Eq. (3).

$$\rho(\theta_s, \theta_v, \varphi) = f_{iso} + f_{geo} k_{geo}(\theta_s, \theta_v, \varphi) + f_{vol} k_{vol}(\theta_s, \theta_v, \varphi) \tag{3}$$

where $\rho(\theta_s, \theta_v, \varphi)$ is the surface reflectance with a θ_s, θ_v, and φ; k_{geo} and k_{vol} are kernels representing the geometric optical mutual shadowing and volumetric scattering components of the surface reflectance, respectively; f_{geo} and f_{vol} are the weights of the two components; and f_{iso} is the isotropic reflectance component. The simulated surface albedo can then be calculated as the hemispherical integration of the surface directional reflectance. Once the regression coefficients in Eq. (1) were obtained using the simulated datasets, the actual surface albedo was estimated using Landsat TOA directional reflectance data. A detailed description of the Landsat albedo estimation can be found in He et al. (2018).

Land surface albedo estimates are dependent on the time of

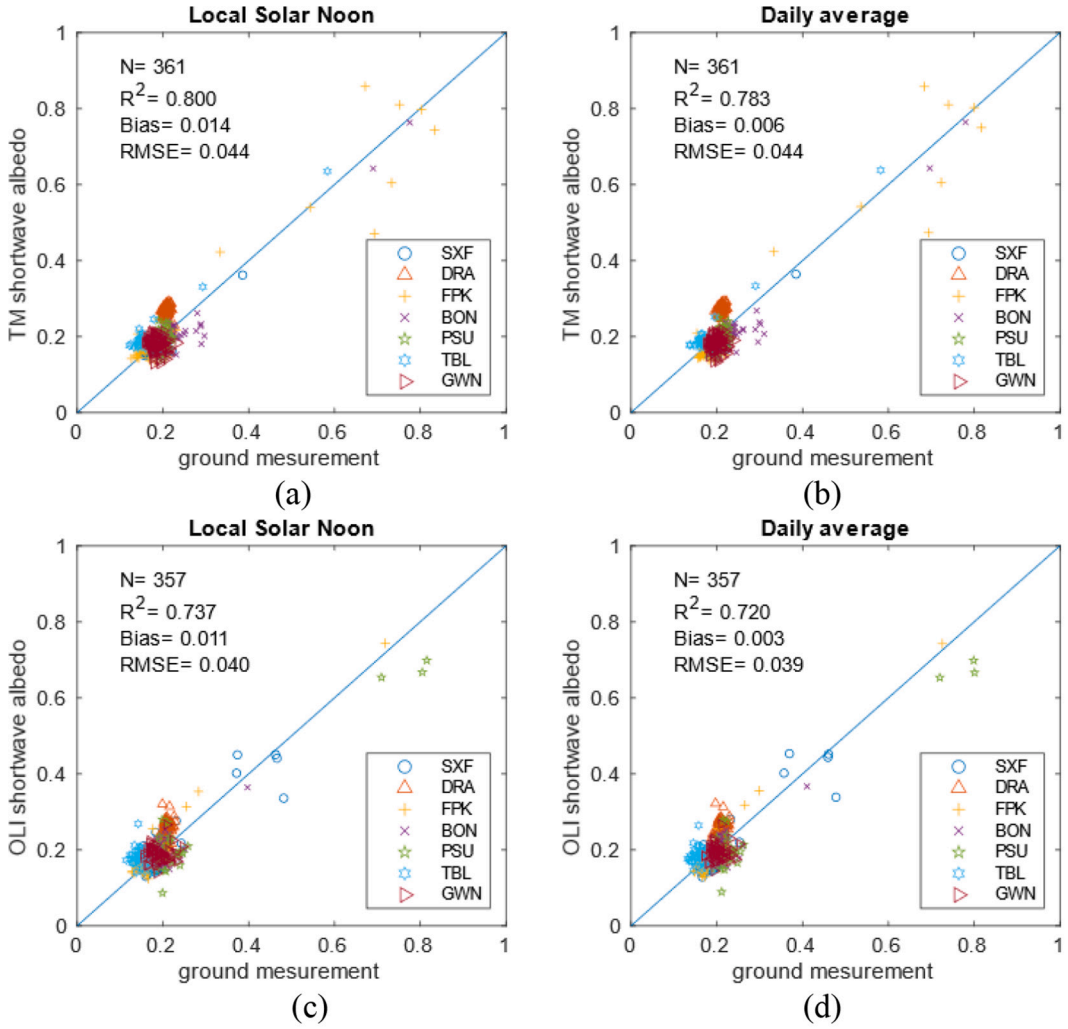

Fig. 5. Relationship between estimated shortwave albedo and ground measurements at SURFRAD sites.

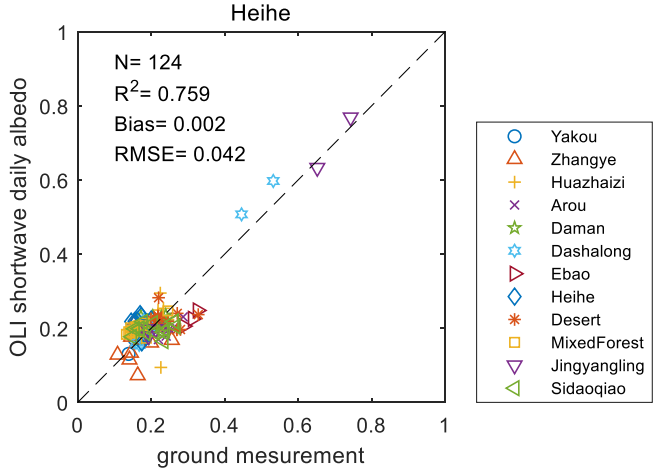

Fig. 6. Relationship between estimated shortwave albedo and ground measurements at Heihe sites.

acquisition and solar zenith angle (SZA) (Liu et al., 2009; Wang et al., 2005; Yang et al., 2008). Over most surfaces, the black-sky albedo (BSA) of the same object decreases with an increase in the SZA, and the BSA at noon is the lowest in the day. The Landsat 5 mission required that the mean local time at any descending node crossing remained constant (between 9:30 and 10:00 a.m.) (Hassett and Johnson, 1984). However, the Landsat 5 orbit was not consistently maintained. Due to orbital drift, the overpass time was delayed from 1995 to 2000 and from 2003 to 2007 (Gao et al., 2014; Zhang and Roy, 2016). This delay involved an acquisition towards local noontime and thereby a smaller SZA at the time of image acquisition. This produced an artificial downward (upward) trend in the instantaneous albedo estimated on the same date of each year.

Landsat orbit drift had certainly an impact when considering long-term series analysis in this study. The instantaneous estimated albedo trend does not reflect real albedo changes due to the inconsistency of the SZA during data acquisition. Therefore, applying an algorithm is mandatory for estimating the average daily and local solar noon albedos. We developed a statistical method (Eqs. (4) and (5)) based on the traditional Landsat DE approach (He et al., 2018) to estimate the local solar noon albedo and daily average albedo to correct for the impact of orbit drift.

$$\alpha_{noon} = \sum \rho_i^{TOA}(\theta_s, \theta_v, \varphi, LAT, DOY)\cdot c_i + c_0 \quad (4)$$

$$\alpha_{daily} = \sum \rho_i^{TOA}(\theta_s, \theta_v, \varphi, LAT, DOY)\cdot c_i + c_0 \quad (5)$$

where α_{noon} and α_{daily} are the daily and local noon surface albedos for the wavelength region of 300-3000 nm; $\rho_i^{TOA}(\theta_s, \theta_v, \varphi, LAT, DOY)$ is the TOA reflectance with a θ_s, θ_v, φ, latitude (LAT), and day-of-year (DOY) for

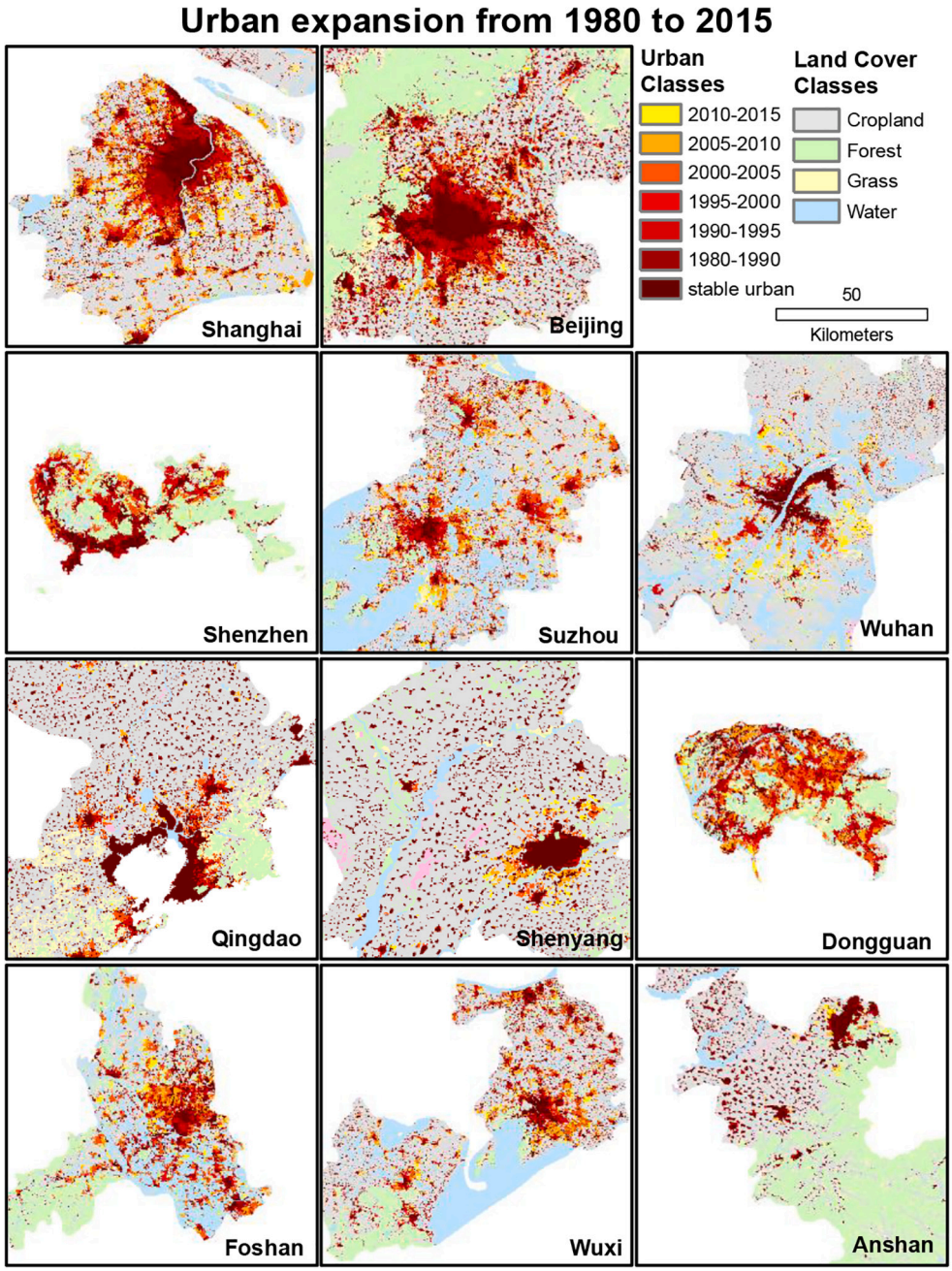

Fig. 7. City land cover and spatial distribution of urban expansion. The first two rows are level 1 cities, and the third and fourth rows are level 2 and level 3 cities, respectively.

Table 5
The transition matrix of land cover change area ratio from 1980s to 2015 (types with change area less than 0.1% are ignored).

2015 1980s	crop	forest	grass	water	built-up
crop	45.58%	0.31%	–	1.22%	8.32%
forest	0.51%	19.40%	–	–	0.90%
grass	0.26%	–	3.10%	–	0.17%
water	0.31%	–	–	8.79%	0.51%
built-up	–	–	–	–	9.33%

spectral band *i*. A flowchart of this method is shown in Fig. 3. The Second Simulation of a Satellite Signal in the Solar Spectrum (6 s) (Vermote et al., 1997) is a set of radiative transfer codes used in this study. Water vapor, ozone, and CO_2 settings are prescribed in the "US62" atmospheric profiles in 6S.

A series of parameters, including BRDF, SZA, latitude (LAT) and day-of-year (DOY) are required to be combined for modeling and estimating the local solar noon and daily mean albedos. Note that the aforementioned relationships between TOA reflectance and local solar noon or daily mean surface albedos are statistical and based on radiative transfer simulations. Compared to the original instantaneous look-up table (LUT) (He et al., 2018), the new LUT (Table 4) included the LAT and the DOY to better account for the spatiotemporal dynamics. Coefficients appearing in Eqs. (4) and (5) are pre-calculated and stored in the two LUTs,

The blue-sky albedo was simulated using the ratio of the surface downward diffuse radiation to the total shortwave radiation, which is a function of the SZA and the aerosol optical depth. The 6S is used to

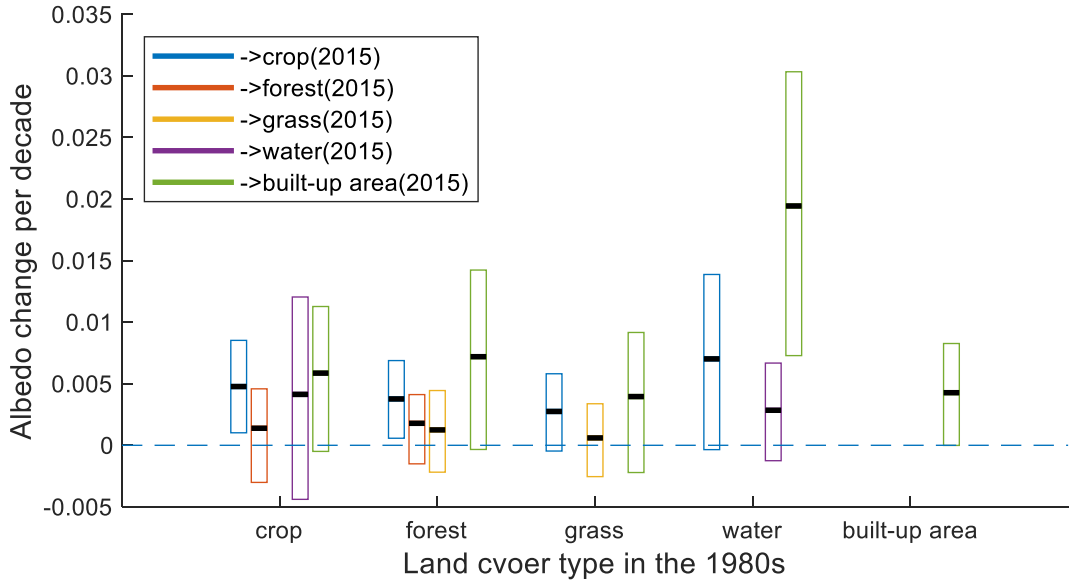

Fig. 8. Albedo change slopes over changed and unchanged land cover types. The changed land cover types were derived from land cover data in the 1980s and 2015. The legend of →crop (2015) means that land cover types in the 1980s was converted to cropland in 2015, and so on. The black line represents the average value. The upper and lower sides of the rectangle correspond to the values of the third quartiles (Q_3) and the first quantiles (Q_1), respectively.

simulate the fraction of diffuse skylight. The blue-sky albedo was calculated as a combination of the BSA and white-sky albedo (WSA), weighted by the sky light ratio factor, as shown in Eq. (6) (Qu et al., 2016). $\rho_{diffuse}$ represents the ratio of the diffuse irradiance to the total downward irradiance.

$$a_{blue-sky} = a_{BSA}\cdot\left(1-\rho_{diffuse}\right) + a_{WSA}\cdot\rho_{diffuse} \tag{6}$$

Daily albedos were calculated as the average instantaneous albedo, weighted by the instantaneous downward fluxes at 30 min intervals (i) during the daytime (Wang et al., 2015), as shown in Eqs. (7) and (8), where $I_d(t_i)$ denotes the instantaneous downward flux at time t.

$$a_{daily} = \sum_i [a(t_i)\cdot w(t_i)\,] \tag{7}$$

$$w(t_i) = I_d(t_i) \Big/ \sum_i I_d(t_i) \tag{8}$$

2.3.2. Trend analyses

Determining the pixel-by-pixel temporal changes in surface albedo relies on an inversion method that consider a least-squares linear regression (Eq. (9)).

$$y_i = b + k_a x_i + \varepsilon \;\; i \in \{1,2,\ldots,N\} \tag{9}$$

where k_a represents the inter-annual change rate of the albedo, b is the intercept, i is the ordinal number of the year, x_i is the year, y_i is the surface albedo value in the i^{th} year, and N represents the number of years. When generating city maps, only pixels with more than 20 years of clear-sky values were used, which exhibited rather stationary trends.

We evaluated the significance of the trend using the F-test. The F-statistic is the test statistic of the regression model. The F-test determines the level of significance of the linear regression between the observed and predicted variables. The P-value indicates the reliability of the fit. The smaller the P-value, the more reliable the change is in the corresponding pixel.

2.3.3. Surface radiative forcing

Radiative forcing (RF) is the difference between the insolation absorbed by the Earth and the energy radiated back to space (Shindell et al., 2013). RF infers changes in the Earth's climate system by altering the Earth's radiative equilibrium and by forcing the temperature to rise or to fall. A positive RF means that the Earth receives more incoming energy from sunlight than it radiates to space, which produces warming, and vice versa. With a changing surface albedo, the upward surface shortwave radiation varies, leading to negative or positive RF.

Surface shortwave RF was calculated by multiplying the change in albedo ($\Delta\alpha$) from 1986 to 2018 by the average value of the multi-year (2001–2008 summer) DSR (DSR_{ave}^{MODIS}), derived from the MODIS DSR product MCD18A1 (Dintwe et al., 2017), using Eq. (10). The change in albedo was calculated using Eq. (11), where α_{T1} represents the average value of the albedo from 1986 to 1990 and α_{T2} represents the average value of the albedo from 2014 to 2018.

$$RF = -\left(\Delta\alpha\cdot DSR_{ave}^{MODIS}\right) \tag{10}$$

$$\Delta\alpha = \alpha_{T2} - \alpha_{T1} \tag{11}$$

3. Results

3.1. Validation of derived surface albedo products

Surface albedos from SURFRAD anchor stations were selected to calculate the correlation between daily and instantaneous albedos. There was a very good correlation between the observed and simulated albedo, as the R^2 value was ~0.99, the bias was less than 0.01, and the RMSE was ~0.01 (Fig. 4). The correlation between the local solar noon albedo and the instantaneous albedo provides similar results. This sustains the derivation of transfer coefficients from the instantaneous observations to local solar noon albedo or daily average albedo.

To ensure that our albedo estimates were dependable, data from the SURFRAD anchor stations and Heihe sites were used to validate the shortwave daily and local solar noon albedo products. The results over the SURFRAD sites are shown in Fig. 5. For noon and daily albedo estimates, the coefficient of determination R^2 was >0.72, with a small bias of ~0.003–0.014 and RMSEs of 0.039–0.044. The results for snow-free cases exhibited bias of 0.002–0.014 and RMSEs of 0.037–0.041. At the Desert Rock (DRA) site, the albedo was slightly overestimated using both TM and OLI data. The overestimations were likely caused by not using the "desert" aerosol type in the radiative transfer simulation as

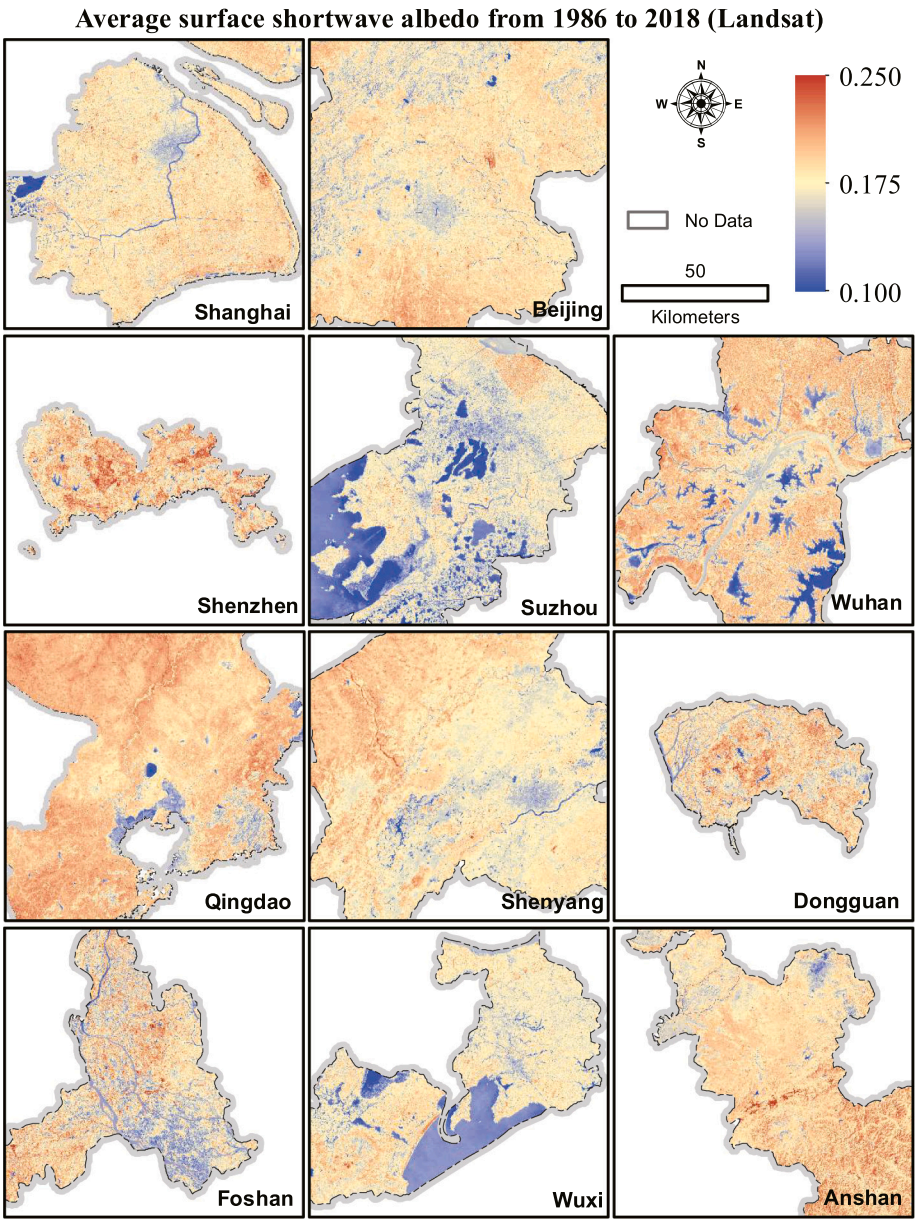

Fig. 9. Average surface shortwave albedo maps of 11 cities in China from 1986 to 2018.

reported in He et al. (2018). For the rest of the sites included in this study, the default "continental" aerosol type adopted in the radiative transfer simulation did not produce any significant systematic errors in albedo estimation.

Fig. 6 shows the validation results over the Heihe sites during in 2016–2017. The albedo accuracy in China was comparable to that at SURFRAD, with a bias of 0.002, an R^2 of 0.759, and a RMSE of 0.042. Such accuracy allows for the reasonable quantification of surface albedo changes due to urbanization in China.

We also chose Lunar Lake (a dry lake playa in Nevada, USA, 38.40°N, 115.99°W Landsat Path/Row 040/033), which has a land cover that has not changed for an extended period, to explore the changes in the correlation coefficient between the solar zenith angle of the Landsat images and surface albedo. For instantaneous, local solar noon, and daily average surface albedos, the R^2 of the correlation with solar zenith angle decreased from 0.062 to 0.013 and 0.011, respectively. This indicates that our method can offset the impact of solar zenith angle changes caused by orbit drift on surface albedo to a certain degree.

3.2. Urban expansion and land cover change

In the past 33 years, the urban land area in China has doubled, and is 4–5 times larger in coastal areas. To understand how cities are changing across China, we sorted the urban class of each pixel by the time it was classified as built-up land. This relies on the assumption that the urbanization process is irreversible (Li et al., 2015); that is, a transition from urban to another land cover type is unlikely. We also included pixels that exhibited reversibility in urbanization to avoid possible errors. Less than 0.3% (±0.1%) of all pixels in each city exhibited this phenomenon, indicating that such a difference can be ignored. The results of urban land expansion in the 11 cities from 1980 to 2015 are shown in Fig. 7. Most of the stable urban regions were located at the center of each city. However, many 'stable urban' areas in the region around the periphery of the city were observed in the northern cities of Qingdao, Shenyang, and Anshan. These are township-gathering areas.

To identify how land cover changes, we counted the pixels that were converted from one land cover type to another from the 1980s to 2015 (Table 5, unclassified land did not count). As a largely agricultural

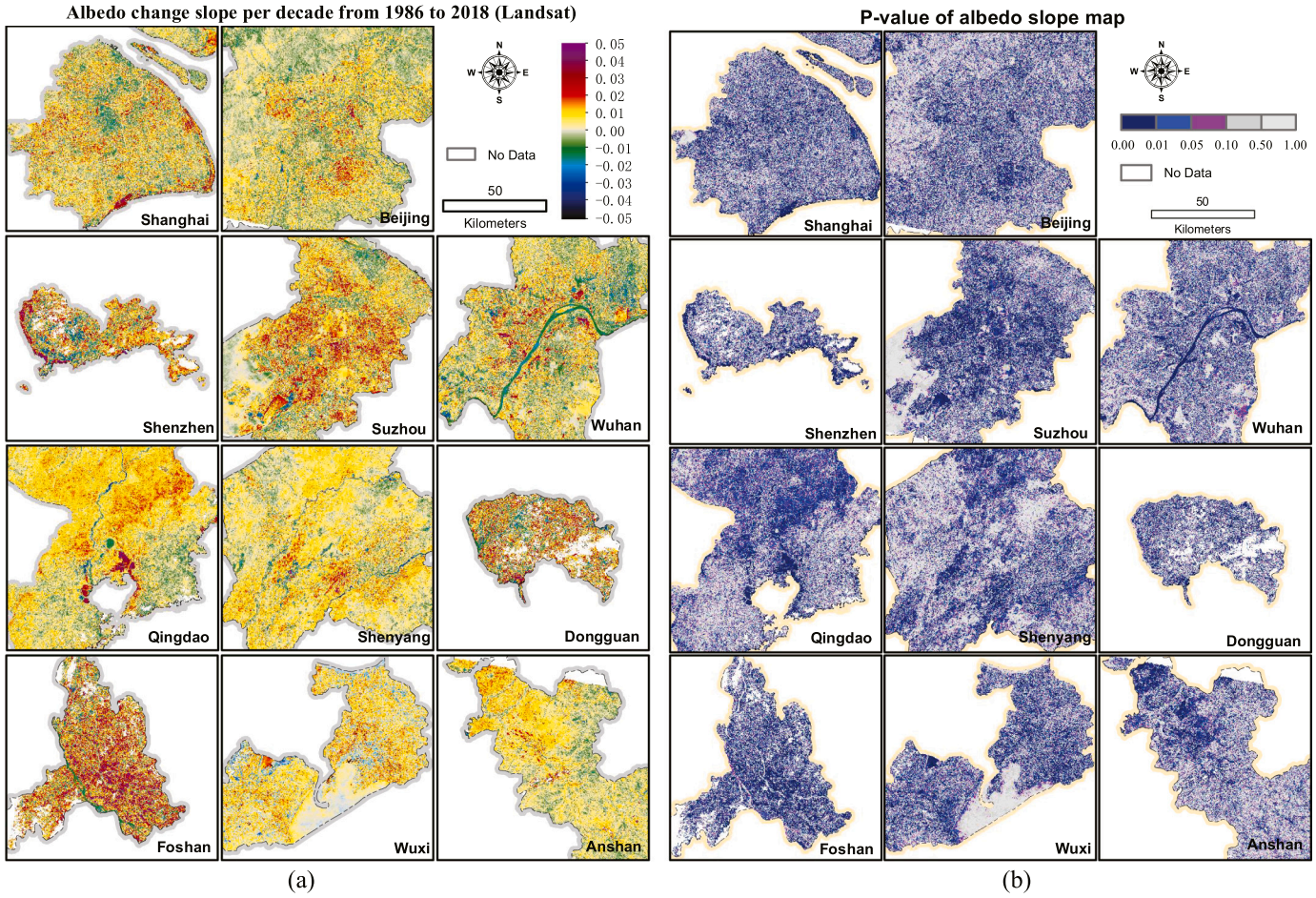

Fig. 10. 1986–2018 Summer albedo change slope per decade and *p*-value maps of 11 cities in China. (a) Landsat as data source; (b) p-value map of (a); (c) GLASS as data source; (d) p-value map of (c).

country, the percentage of cultivated land is the highest (45–55%) in the majority of Chinese cities, followed by forest and built-up land. Nevertheless, most areas (~86.2%) did not experience significant land transformations over the past three decades. Among the land cover type conversions, the conversion from cropland to built-up land was the largest (up to 8.32%).

Land cover change is one of the main factors that causes changes in surface albedo (Hu et al., 2019; Tang et al., 2018). We determined the slope characterizing the albedo changes over time to better understand the impacts of land cover conversions on albedo (Fig. 8). The albedo increased the most in areas where a conversion from water to built-up land occurred. However, this only depicts a small proportion of all the pixels. Fig. 8 shows that cropland albedo had a slightly increasing trend and that the increasing trend for the conversion of cropland to built-up land was larger. However, croplands in/around cities are usually small and fragmented, and the crop types grown there are variable, resulting in unstable land cover classification accuracy. The resulting crop albedo trend analysis may not be reliable, which requires future exploration. Moreover, the albedo of pixels converted from other types of land cover to built-up land increased more than any other land conversion type, although there was also an overall increase in albedo.

3.3. Spatiotemporal changes of urban surface albedo

As shown in Fig. 9, the average multi-year albedo in the central urban areas (e.g. Fig. 7) of most cities was lower than that of its surroundings, except in Shenzhen and Dongguan.

To highlight the spatiotemporal patterns of albedo changes in the study area, Landsat and GLASS data were selected with the closest dates as possible, and the albedo trends were calculated using the method described in Section 2.3.2. Fig. 10(a) shows the slope of the albedo obtained from the regression of every pixel of the Landsat images from 1986 to 2018. Fig. 10(c) shows the slope calculated using the GLASS data. In total, 59% of the areas exhibited increasing trends in albedo and 22% of the areas exhibited decreases in albedo. Cities with longer durations of urbanization, such as Beijing, Shanghai and Wuhan, had more than 28% of the built-up land exhibiting decreasing trends, which is twice the area in other cities. The Landsat albedo of the Pearl River Delta cities (Shenzhen, Foshan, and Dongguan) increased significantly, with all values being above average. Cities such as Shenzhen and Foshan rapidly developed after reforms in the late 1980s. The newly constructed buildings and roads lead surface albedo rose significantly (Hamoodi et al., 2019).

The ranges of albedo trends for each city are shown in Fig. 11. In the 11 study cities, the spatial distribution and overall statistics of trends derived from the Landsat and GLASS data were generally similar in most regions, especially in areas with steep slopes. On the pixel level, the trends derived from Landsat can reach from −0.03 to 0.06 per decade, while trends derived from GLASS are mostly between −0.01 to 0.01. The magnitude of the albedo trend derived from 30 m Landsat data is generally 2.1 to 4.8 times greater than that derived from the 0.05-degree GLASS data. The absolute trends estimated from high-resolution Landsat albedos are larger, which can reflect more details in terms of spatial heterogeneity over the urban landscape. The spatially aggregated

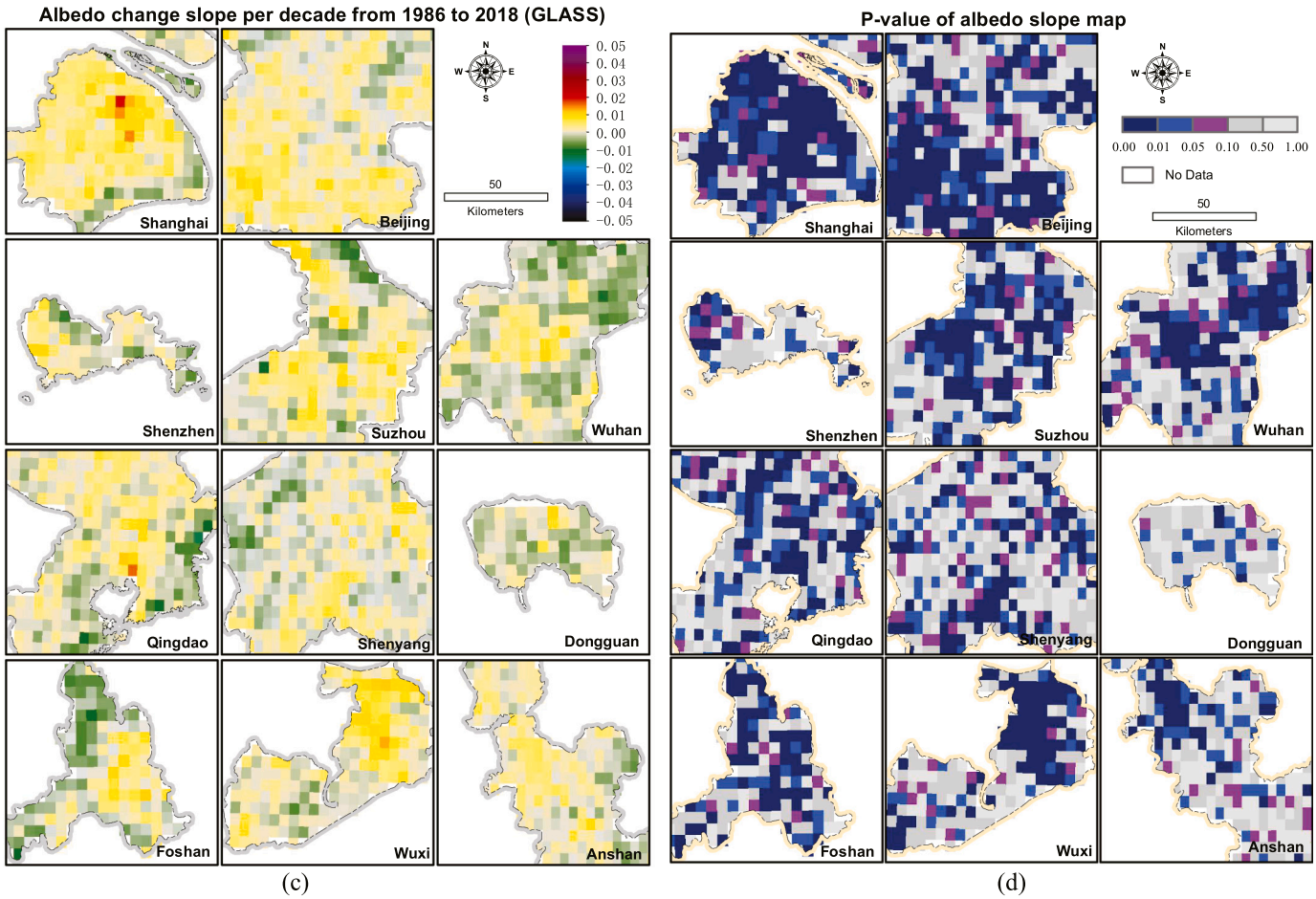

Fig. 10. (*continued*).

Landsat albedo values at 0.05-degree was also added into the inter-comparison in Fig. 11. In general, the statistics of 0.05-degree aggregated Landsat albedo values were very close to those from the 0.05-degree GLASS product, which demonstrates a good agreement between these two datasets at the 0.05-degree scale. Small albedo differences between these two datasets can still be observed, which may be attributed to the difference in their sensor calibrations, retrieval algorithms, and temporal aggregations. Nevertheless, the difference between the two products at 0.05-degree scale was much smaller than the difference between statistics calculated at two different scales (30 m and 0.05-degree). As a result, the average value with Landsat of all the study cities was 3.6 times larger than that from the GLASS albedo product. It comes out that studies using coarse-resolution data may underestimate the impact of urbanization, as well as the role of growing cities on climate change. This clearly emphasizes the need for high-resolution sensors.

By comparing the two data sources, it appears that albedo maps generated using Landsat data contained interesting features. One block in a city is a single pixel in the GLASS images. However, lines of streets or boundaries of buildings can be observed in the Landsat images. The roads produce a smaller change in albedo than the adjacent roof because they use black asphalt, which is a low-albedo material. This kind of detail is meaningful with regard to urban development. It is worth noting that an increase in albedo was observed in the center of Shanghai and a ring-shaped albedo reduction zone was observed at the edge of the center of the city, the magnitude of which was approximately-0.0199 per decade. A comparable decrease approximately −0.0126, was also observed in Suzhou (Fig. 10(a)). These features would not be visible in coarse-resolution datasets. The Yangtze River running through Wuhan even exhibited a strong albedo trend. However, the overall trend was not affected by changes in the river because the river area was only 2.25% of the whole city of Wuhan.

To explore the differences in the albedo changes of the built-up land during different time periods, we calculated the mean, first quartile and third quartile of the albedo slope for each urban class, as shown in Fig. 12. The albedo of the newer built-up land increased compared to the albedo of the built-up land that has existed for a longer period. It is worth emphasizing that the albedo slopes of the different urban classes in most cities had ‘U-shaped’ trends. In other words, the slope of the ‘stable’ area had more positive changes than that of the ‘1980–1990’ and ‘1990–1995’ areas. This is due to the positive impacts of the reconstructed internal structure of the ‘stable’ areas or the renovation of surface materials used for urban development.

3.4. Details of time series changes in urban surface albedo

The region of interest (ROI) presented in Fig. 13 indicates industrial zones that occurred in nearly all Chinese cities. The ROI was 1 km^2. The conversion of cultivated land to built-up land has led to sudden increases in albedo. In 2005, a significant turning point was detected using a piecewise regression approach (Chen et al., 2014; Wang et al., 2011). According to Google Earth images, 2005 was when building construction really began. One reason for the increase in albedo is that most of the factory buildings were low, and the building density was not high. Another reason is that the roof layer was mostly light-colored steel with a strong reflectance (Hamoodi et al., 2019). The correlation between surface albedo and NDVI (derived from NIR SR minus red SR divided by their total) at the regional scale was −0.707, exhibiting a strong negative correlation as long-term construction replaced the original

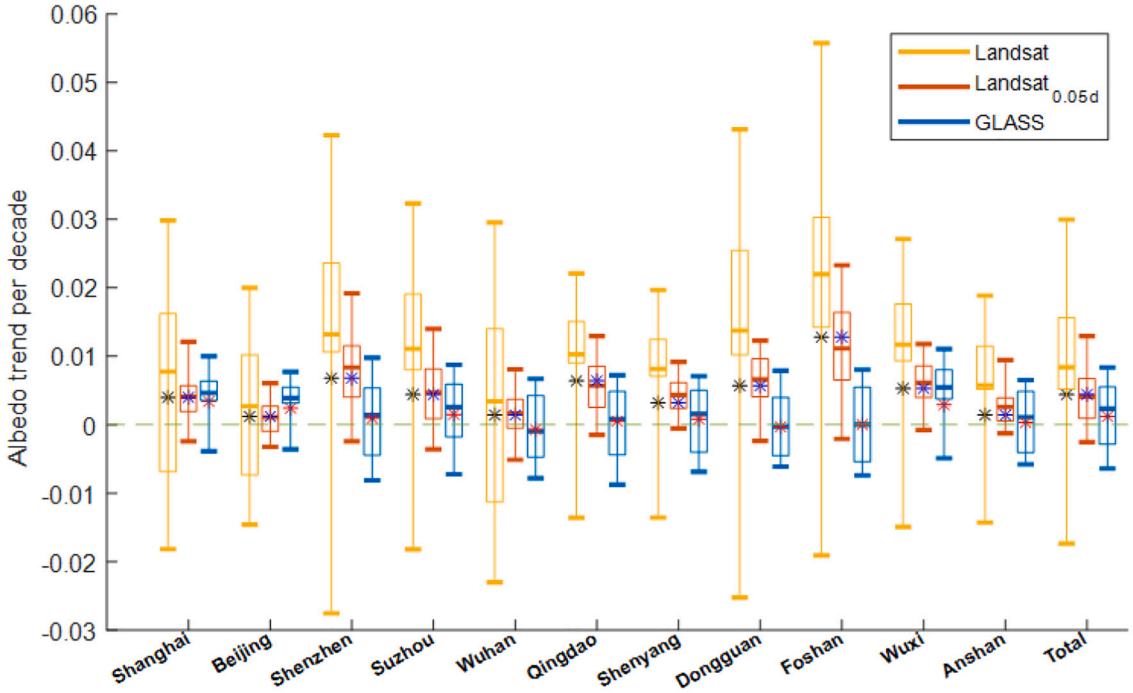

Fig. 11. Comparison chart of albedo trend magnitude per decade of each city derived from Landsat at 30 m (left, yellow lines with black '*'), Landsat aggregated to 0.05-degree (middle, red lines with blue '*'), and GLASS at 0.05 degree (right, blue lines with red '*'). The top and bottom horizontal lines represent 95% and 5% of the values respectively. The upper and lower sides of the rectangle correspond to the values of the third quartiles (Q3) and the first quantiles (Q1). The horizontal line in the rectangle represents the average of the albedo trend of all pixels. The '*' indicates the albedo trend in the aggregate. (For interpretation of the references to colour in this figure legend, the reader is referred to the web version of this article.)

cultivated land. The NDVI decreased as the vegetated areas were subsumed by buildings and roads.

A ring-shaped descending zone was observed in Shanghai and Suzhou (Fig. 14). As shown in Fig. 14(f), the NDVI decreased rapidly from 1986 to 2000, but increased slowly after 2000. According to Google Earth images, the construction period occurred before 2000. After 2000, the main areas of the regional construction did not change significantly. The correlation coefficient between the surface albedo and NDVI from 2000 to 2015 was −0.581, indicating that vegetation growth was one major reason for the decrease in albedo. In addition, the aging of surface materials (such as concrete and asphalt) may lead to changes in albedo (Hamoodi et al., 2019; Shi et al., 2019). The road material in the ROI was also converted from cement to asphalt, which has a much lower albedo.

The albedos in the central urban areas of Shanghai, Suzhou, and Wuxi exhibited slight increasing trends. Fig. 15 shows the details of the ROI in central Shanghai. The downtown area of Shanghai is mainly located on the western side of the Huangpu River and was already a bustling area in the mid-20th century. In the 1980s, the planar expansion stage ended, and urban development mostly consisted of internal urban reconstruction. The correlation coefficient between the surface albedo and NDVI in the ROI was 0.289, possibly because the green areas located in central Shanghai are too small to have a significant effect on the albedo. However, the albedo in the central area (old district) exhibited decreasing trends in Beijing, Shenyang, Wuhan, etc. This phenomenon, which was not present in all cities, may be due to aging materials (Ban-Weiss et al., 2015; Kalantar et al., 2017), shadows, and increase in the vegetation fraction.

3.5. Surface radiative forcing

The spatial distributions of radiative forcing (RF) caused by albedo changes in all study areas over the past 33 years are shown in Fig. 16. Because DSR does not vary drastically in space, the spatial distribution of the RF was consistent with changes in albedo, except for data losses caused by the MODIS DSR product.

The average RF for each city is listed in Table 6. The 33-year average RF value of all cities was negative (approximately −7.757 W/m^2). Foshan had the most negative RF (−29.359 W/m^2), while Beijing had the least negative RF (−0.475 W/m^2). Ignoring factors such as anthropogenic heat emissions, the urbanization process has a cooling effect on cities from an albedo perspective.

Moreover, we also used a piecewise regression approach (Chen et al., 2014; Wang et al., 2011) to detect possible turning points (TPs) in the inter-annual changes in annual mean albedo of the study areas from 1986 to 2018. The RF caused by changes in albedo before and after a possible TP in each city is also listed in Table 6. Cities such as Wuhan exhibited positive RFs before a possible TP, then negative RFs afterward; however, Foshan exhibited negative RFs both before and after a possible TP. These results indicate that with urban development in a city, the RF may first turn positive and then negative.

In addition, the biogeophysical impacts of albedo fluctuations should be considered in climate model simulations. Insolation budgets affected by changes in albedo would probably alter the local climate. This could include an enhancement of the UHI effect due to a decrease of the albedo.

4. Discussion

4.1. Albedo estimation method

The DE method has a high retrieval rate and does not require ancillary data inputs, which is preferable for high-resolution satellite data with a low frequency of revisit. The algorithm was validated on a variety of land cover types and climate regions (He et al., 2017; Liang et al., 2005). The validation results had satisfactory estimation accuracies with RMSEs of less than 0.044 and good temporal continuity for albedos estimated from the different Landsat sensors (e.g., TM and OLI) (He et al., 2018). The application of the temporal estimations over urban

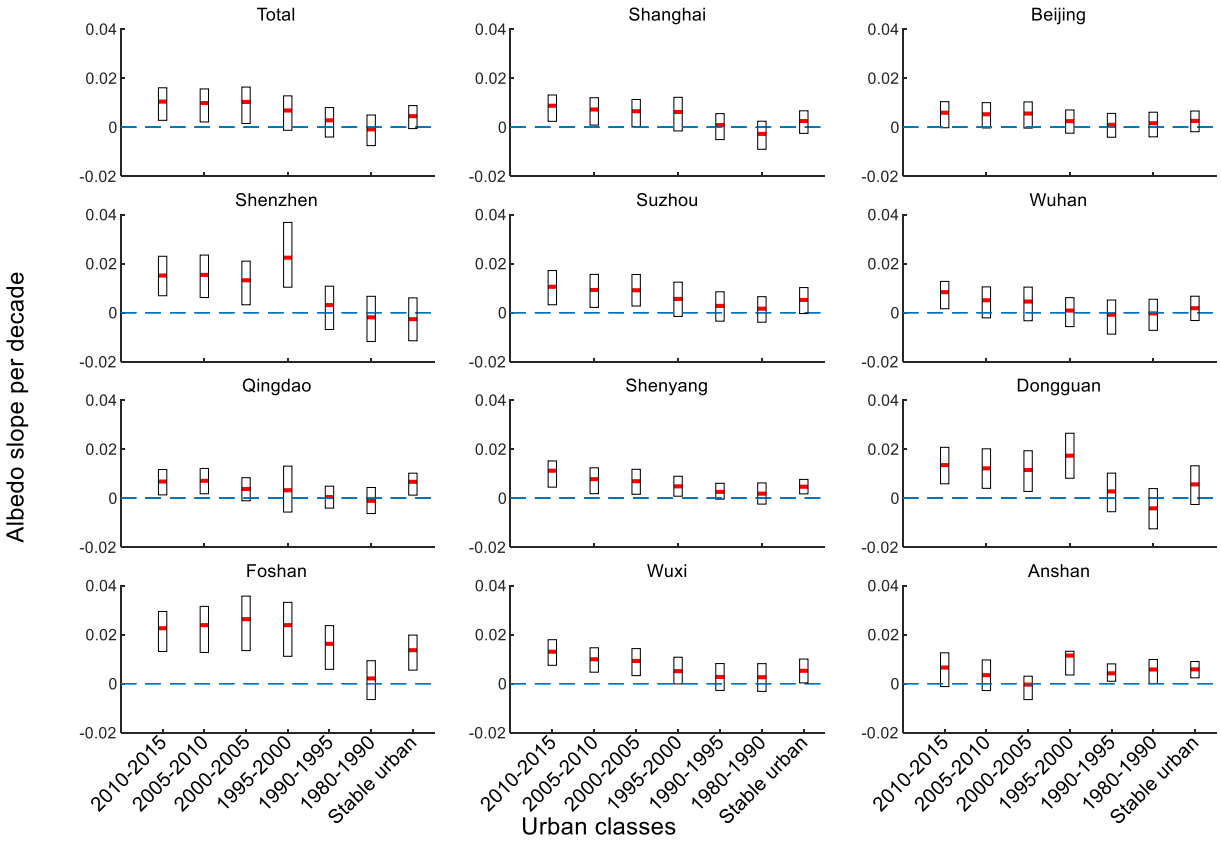

Fig. 12. The slope of albedo change in different urban classes, corresponding to the urban classes shown in Fig. 7. The red line represents the average value. The upper and lower sides of the rectangle correspond to the values of the third quartiles (Q_3) and the first quantiles (Q_1), respectively. (For interpretation of the references to colour in this figure legend, the reader is referred to the web version of this article.)

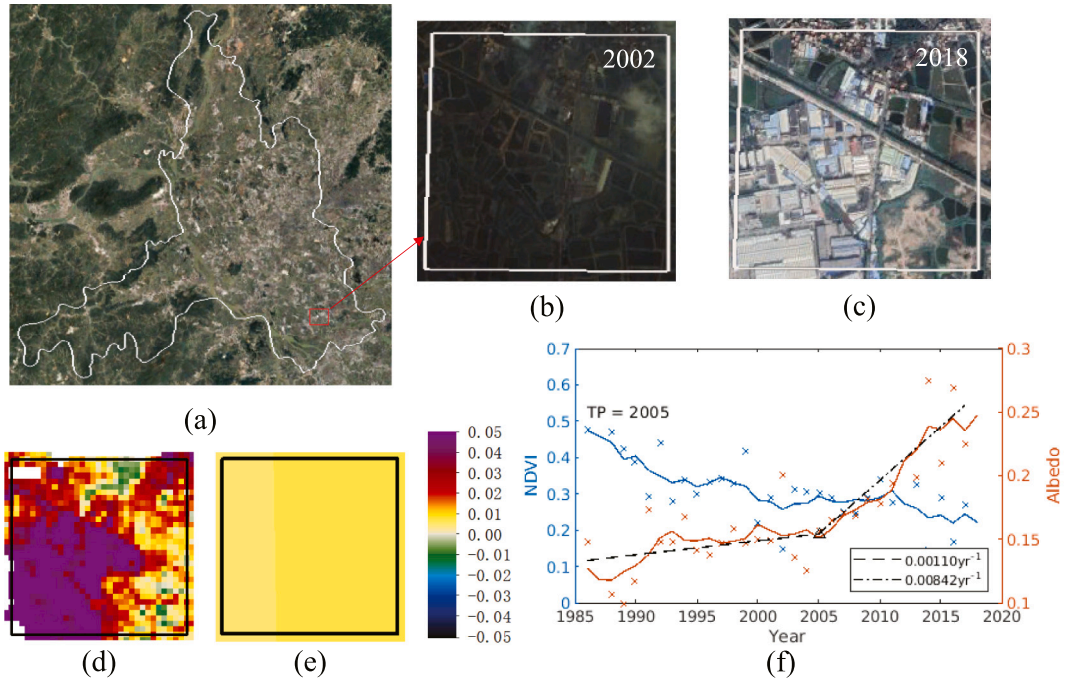

Fig. 13. Region of interest (ROI) in new built-up area in Foshan: (a) Image from Google Earth, white lines represent the boundaries of the city, the red box represents ROI; (b) and (c) Detailed map of ROI (red box area shown in (a)) on Google Earth, the number in the upper right corner represents the year of acquisition; (d) Landsat ROI albedo change details; (e) GLASS ROI albedo change details; (f) The moving average method was used to show the trend of albedo and NDVI variation of ROI. The solid curve corresponds to annual rolling average (using a 5-year moving window). (b), (c), (d) and (e) represent the same area of 1 km^2. (For interpretation of the references to colour in this figure legend, the reader is referred to the web version of this article.)

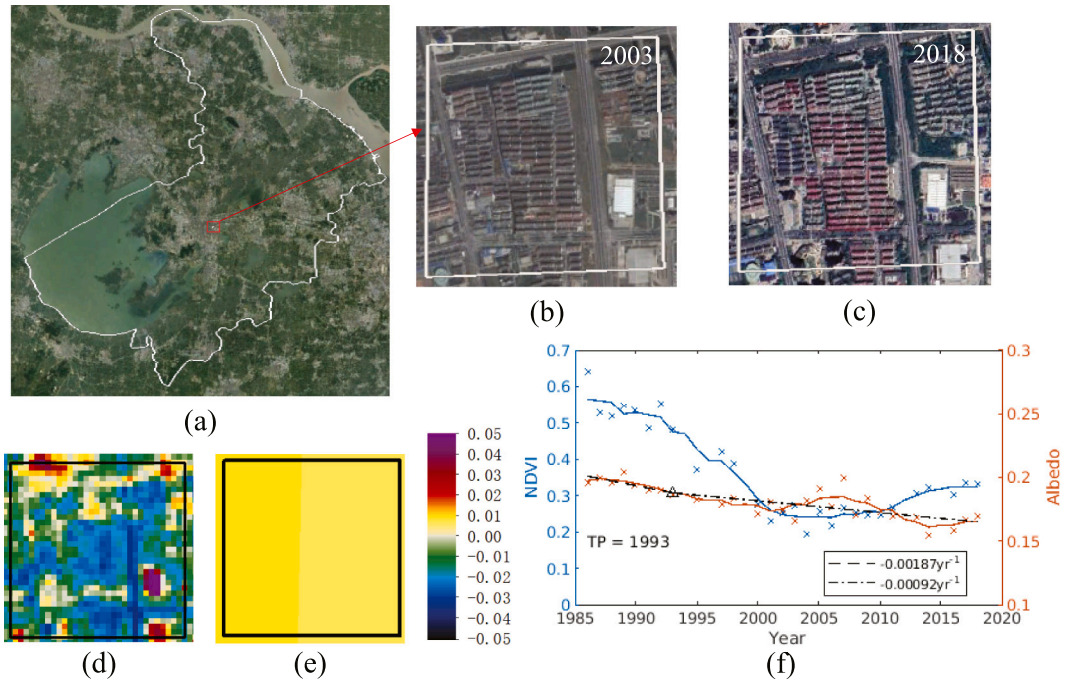

Fig. 14. Similar to Fig. 13 but for fringe drop zone in Suzhou.

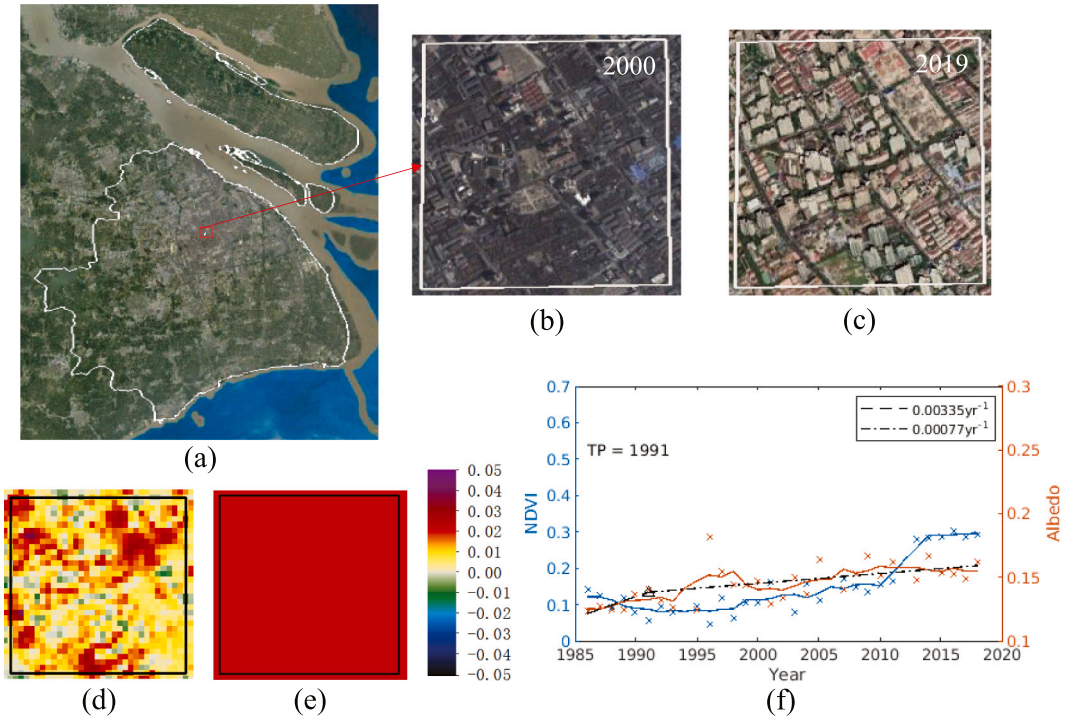

Fig. 15. Similar to Fig. 13 but for central area in Shanghai.

areas should be reliable particularly for temporal analyses. Due to the lack of ground measurements of surface albedo over urban areas, an unmanned aerial vehicle (UAV) carrying instruments is likely the best option for measuring at the fine-scale surface albedo of urban environment at different times (Cao et al., 2018). Baldinelli et al. (2017) used albedometer measurements for verification and improved two satellite albedo estimation algorithms. In addition, the three-dimensional structure of a city forms a complex system and a well-defined BRDF dataset is required to improve the accuracy of urban albedo assessments made through modeling.

Because the temporal distribution of cloud-free Landsat data is sparse (only one image every 16 days), we only selected images acquired during the summer to avoid possible errors caused by image acquisition at different seasons. In the future, more data sources such as the Système Probatoire d'Observation de la Terre (SPOT) archive data sets should be utilized. Combining multi-source satellite data sets could result in an enhanced trend, while the overall tendency (positive or negative) should not be affected.

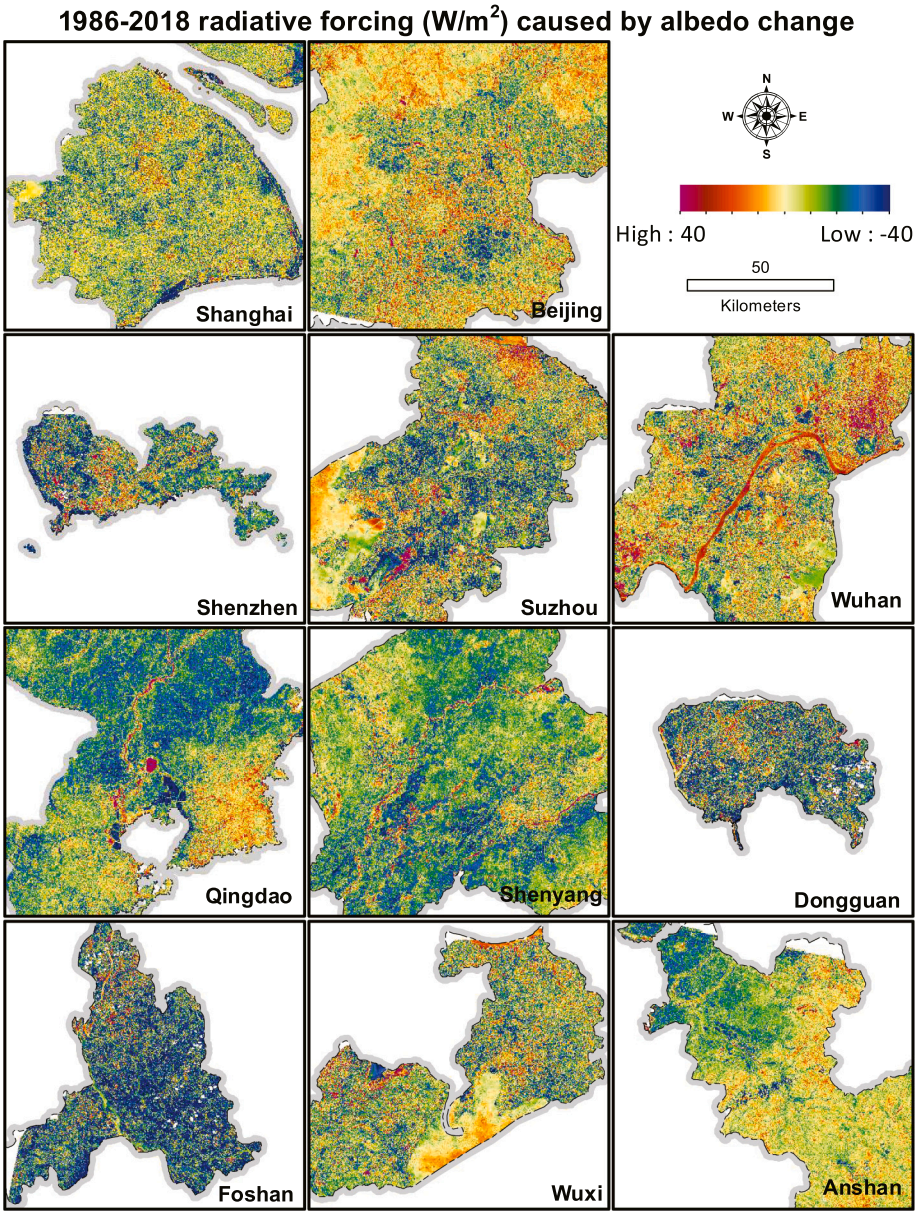

Fig. 16. 1986–2018 radiative forcing caused by albedo change.

Table 6
Average Radiative Forcing (W/m^2) from 1986 to 2018, before and after the possible TP.

City Names	Whole Area RF	TP	RF before TP	RF after TP
Shanghai	−7.259	1996	−4.794	−2.465
Beijing	−0.475	1993	5.401	−5.877
Shenzhen	−15.029	2009	−15.224	0.195
Suzhou	−6.164	2006	−10.505	4.341
Wuhan	−0.542	1990	3.271	−3.813
Qingdao	−14.523	2008	−4.691	−9.837
Shenyang	−12.336	1990	−3.379	−8.957
Dongguan	−18.043	2012	−9.529	−8.514
Foshan	−29.359	2007	−16.251	−13.108
Wuxi	−7.054	1991	−12.563	5.509
Anshan	−4.760	2008	4.429	−9.189
Total Average	−7.757			

4.2. Time series analysis

The urbanization process is accompanied by the rapid expansion of the imperviousness and shrinkage of natural surfaces, most of which have been converted from cropland to built-up land (Table 5). When land cover was transformed from a natural surface to urban land, the surface albedo increased in 21% of the areas, while it only decreased in 5% of the areas (Fig. 8). Compared to coarser-resolution MODIS data, the Landsat data highlighted the impacts of small-scale land cover changes on albedo. Indeed. there is an urgent need to better identify which are the main drivers behind this land cover change process in relation to albedo as a reference for future albedo modification that are in line with expected recommendations.

The trends derived from the Landsat and GLASS data were generally similar in most regions. However, the absolute slopes estimated from the high-resolution Landsat albedo were larger than those estimated from the coarse-resolution GLASS albedo. Coarse-resolution data, especially products with kilometer-scale resolution, cannot reflect the distribution of albedo and its temporal changes at an urban block scale. The positive

and negative changes in high-resolution and small-scale observations could hide each other in coarse-resolution observations. The trends derived from the GLASS and Landsat data were the same because the albedo is a linearly process that can be scaled at various temporal and spatial resolutions. However, the average values of the trends obtained from datasets with different resolutions cannot be calculated by simply using linear scale conversion, because of the non-linear relationship/process in the estimation algorithm. The scale issue is rather complex and requires further investigation.

This study only discussed the relationship between land surface albedo and land cover in cities. However, changes in albedo could be influenced by other factors (tree canopy cover, surface materials etc.). Future research work should explore the detection versus attribution factors that are the main drivers of albedo changes. This will reinforce our understanding of the influence of surface albedo on regional and global climate change. In addition, the relationship between urban albedo and urban canopy structure should be investigated by introducing the Digital Surface Model (DSM) (Landier et al., 2016; Mohajeri et al., 2019). The combined impacts of the urban landscape and albedo changes on urban microenvironments should also be investigated (Alchapar and Correa, 2016; Morini et al., 2018; Xu et al., 2020). Earth observations can also provide constraints for the radiative description of urban surfaces for numerical studies of surface energy flux or for urban climate models that simulate energy exchange in complex urban canopies.

Comparing the stage of urban development and the changes in the city's albedo, we observed that cities with medium-sized populations generally exhibited faster increase in albedo. Owing to the different levels of heterogeneity among cities, it is difficult to classify them based on a single indicator. Analyzing the temporal changes in albedo and the difference in RF before and after a turning point yielded some interesting recurring features. Provided that most cities in China will continue to expand according to the current scenario, urban albedo in general should follow the same trend, which involves an initial decrease followed by an increase, and yields a negative contribution to RF.

5. Conclusion

In this study, we refined the method previously used for estimating the instantaneous surface albedo to derive the daily average albedo from Landsat data. The use of daily average albedos can offset the influence of TM orbit drift on the albedo trend to a certain degree. This further allowed us to explore the inter-annual changes of the surface albedo.

We used both Landsat and GLASS data to quantitatively assess the surface albedo trends in various districts of expanding cities in China during the same time period. We found that Landsat data exhibited a larger albedo trend magnitude (3–4 times on average) compared to GLASS data. As expected, the coarse-resolution satellite data underestimated the actual changes due to the spatial heterogeneity of the urban land surface. The findings revealed an increase in albedo of $+0.0044$ per decade (based on Landsat) in the study areas from 1986 to 2018, with an average radiative forcing of -7.757 W/m^2. Decreases in absorbed solar energy means that urbanization has a cooling effect. Such an increase in surface albedo rise is linked to the conversion of land cover types during urbanization. The conversion of natural surfaces to bright and sparse buildings leads to an increase in albedo. However, the conversion of natural surfaces to dark and dense buildings reduces the albedo. Accompanying the development of cities, increases in urban green areas will also cause a decrease in surface albedo. In the lifetime of an expanding city, the associated albedo exhibits a reduction before reaching a peak.

In summary, the main goal of this study was to address the knowledge gap regarding changes in surface albedo in 11 Chinese cities over the past 33 years, as well as the relationship between albedo and land cover characteristics. This study offers an analysis of high-resolution satellite data to better understand how the albedo of cities at different development stages and from contrasting climatic zones varies over an extended period of time. Understanding the spatiotemporal differences in albedo maps will help us perform additional research on urban climate change and UHIs, as they can produce major issues for health of the residents. This study also provides a useful tool for managing energy consumption over cities undergoing permanent land cover transformations.

Declaration of Competing Interest

The authors declare that they have no known competing financial interests or personal relationships that could have appeared to influence the work reported in this paper.

Acknowledgments

This research is supported by the National Natural Science Foundation of China (Grant No. 42090012 and 41771379) and Hubei Province Natural Science Foundation (Grant No. 2021CFA082). We also like to thank for the support by the National Earth System Science Data Center, National Science & Technology Infrastructure of China (http://www.geodata.cn) for product development and data dissemination. We want to acknowledge USGS for offering Landsat L1 product freely download. We thank GLASS team for providing shortwave surface albedo product. We would like to acknowledge MODIS team for making DSR products available for research purpose. We thank SURFRAD and Heihe observation network for providing invaluable field measurements. We acknowledge RESDC providing the LUCC database.

References

Akbari, H., Menon, S., Rosenfeld, A., 2009. Global cooling: increasing world-wide urban albedos to offset CO2. Clim. Chang. 94, 275–286.
Akbari, H., Matthews, H.D., Seto, D., 2012. The long-term effect of increasing the albedo of urban areas. Environ. Res. Lett. 7, 024004.
Alchapar, N.L., Correa, E.N., 2016. The use of reflective materials as a strategy for urban cooling in an arid "OASIS" city. Sustain. Cities Soc. 27, 1–14.
Ali, R., Bakhsh, K., Yasin, M.A., 2019. Impact of urbanization on CO2 emissions in emerging economy: evidence from Pakistan. Sustain. Cities Soc. 48, 101553.
Augustine, J.A., DeLuisi, J.J., Long, C.N., 2000. SURFRAD–a national surface radiation budget network for atmospheric research. Bull. Am. Meteorol. Soc. 81, 2341–2358.
Augustine, J.A., Hodges, G.B., Cornwall, C.R., Michalsky, J.J., Medina, C.I., 2005. An update on SURFRAD—the GCOS surface radiation budget network for the continental United States. J. Atmos. Ocean. Technol. 22, 1460–1472.
Bagan, H., Yamagata, Y., 2014. Land-cover change analysis in 50 global cities by using a combination of Landsat data and analysis of grid cells. Environ. Res. Lett. 9, 064015.
Baldinelli, G., Bonafoni, S., Rotili, A., 2017. Albedo retrieval from multispectral Landsat 8 observation in urban environment: algorithm validation by in situ measurements. IEEE J. Select. Top. Appl. Earth Observ. Remote Sens. 10, 4504–4511.
Ban-Weiss, G.A., Woods, J., Millstein, D., Levinson, R., 2015. Using remote sensing to quantify albedo of roofs in seven California cities, part 2: results and application to climate modeling. Sol. Energy 115, 791–805.
Barnes, C.A., Roy, D.P., 2010. Radiative forcing over the conterminous United States due to contemporary land cover land use change and sensitivity to snow and interannual albedo variability. J. Geophys. Res. Biogeosci. 115.
Cai, H., Wang, J., Feng, Y., Wang, M., Qin, Z., Dunn, J.B., 2016. Consideration of land use change-induced surface albedo effects in life-cycle analysis of biofuels. Energy Environ. Sci. 9, 2855–2867.
Cao, C., Lee, X., Muhlhausen, J., Bonneau, L., Xu, J., 2018. Measuring landscape albedo using unmanned aerial vehicles. Remote Sens. 10, 1812.
Chander, G., Markham, B., 2003. Revised Landsat-5 TM radiometric calibration procedures and postcalibration dynamic ranges. IEEE Trans. Geosci. Remote Sens. 41, 2674–2677.
Chander, G., Helder, D.L., Markham, B.L., Dewald, J.D., Kaita, E., Thome, K.J., Micijevic, E., Ruggles, T.A., 2004. Landsat-5 TM reflective-band absolute radiometric calibration. IEEE Trans. Geosci. Remote Sens. 42, 2747–2760.
Chander, G., Markham, B.L., Helder, D.L., 2009. Summary of current radiometric calibration coefficients for Landsat MSS, TM, ETM+, and EO-1 ALI sensors. Remote Sens. Environ. 113, 893–903.
Chapman, S., Thatcher, M., Salazar, A., Watson, J.E., McAlpine, C.A., 2019. The impact of climate change and urban growth on urban climate and heat stress in a subtropical city. Int. J. Climatol. 39, 3013–3030.
Chen, B., Xu, G., Coops, N.C., Ciais, P., Innes, J.L., Wang, G., Myneni, R.B., Wang, T., Krzyzanowski, J., Li, Q., Cao, L., Liu, Y., 2014. Changes in vegetation photosynthetic activity trends across the Asia–Pacific region over the last three decades. Remote Sens. Environ. 144, 28–41.

Claverie, M., Vermote, E.F., Franch, B., Masek, J.G., 2015. Evaluation of the Landsat-5 TM and Landsat-7 ETM+ surface reflectance products. Remote Sens. Environ. 169, 390–403.
Dintwe, K., Okin, G.S., Xue, Y., 2017. Fire-induced albedo change and surface radiative forcing in sub-Saharan Africa savanna ecosystems: implications for the energy balance. J. Geophys. Res.-Atmos. 122, 6186–6201.
Feng, H., Dong, H., Chen, C., Meng, Q., An, G., 2012. The variation analysis of land surface albedo in Beijing in recent ten years. In: 2012 IEEE International Geoscience and Remote Sensing Symposium. IEEE, pp. 6309–6312.
Feng, Y., Du, S., Myint, S.W., Shu, M., 2019. Do urban functional zones affect land surface temperature differently? A case study of Beijing, China. Remote Sens. 11, 1802.
Friedlingstein, P., Jones, M., O'Sullivan, M., Andrew, R., Hauck, J., Peters, G., Peters, W., Pongratz, J., Sitch, S., Le Quéré, C., 2019. Global carbon budget 2019. Earth Syst. Sci. Data 11, 1783–1838.
Gao, F., He, T., Masek, J.G., Shuai, Y., Schaaf, C.B., Wang, Z., 2014. Angular effects and correction for medium resolution sensors to support crop monitoring. IEEE J. Select. Top. Appl. Earth Observ. Remote Sens. 7, 4480–4489.
Georgescu, M., Moustaoui, M., Mahalov, A., Dudhia, J., 2013. Summer-time climate impacts of projected megapolitan expansion in Arizona. Nat. Clim. Chang. 3, 37–41.
Georgescu, M., Morefield, P.E., Bierwagen, B.G., Weaver, C.P., 2014. Urban adaptation can roll back warming of emerging megapolitan regions. Proc. Natl. Acad. Sci. U. S. A. 111, 2909.
Gong, P., Liang, S., Carlton, E.J., Jiang, Q., Wu, J., Wang, L., Remais, J.V., 2012. Urbanisation and health in China. Lancet 379, 843–852.
Guan, X., Wei, H., Lu, S., Dai, Q., Su, H., 2018. Assessment on the urbanization strategy in China: achievements, challenges and reflections. Habit. Int. 71, 97–109.
Güneralp, B., Reba, M., Hales, B.U., Wentz, E.A., Seto, K.C., 2020. Trends in urban land expansion, density, and land transitions from 1970 to 2010: a global synthesis. Environ. Res. Lett. 15, 044015.
Hamoodi, M.N., Corner, R., Dewan, A., 2019. Thermophysical behaviour of LULC surfaces and their effect on the urban thermal environment. J. Spat. Sci. 64, 111–130.
Hassett, P., Johnson, R., 1984. LANDSAT-5 Orbit Adjust Maneuver Report.
He, T., Liang, S., Wang, D., 2017. Direct estimation of land surface albedo from simultaneous MISR data. IEEE Trans. Geosci. Remote Sens. 55, 2605–2617.
He, T., Liang, S., Wang, D., Cao, Y., Gao, F., Yu, Y., Feng, M., 2018. Evaluating land surface albedo estimation from Landsat MSS, TM, ETM +, and OLI data based on the unified direct estimation approach. Remote Sens. Environ. 204, 181–196.
Hong, J.-W., Hong, J., Chun, J., Lee, Y.H., Chang, L.-S., Lee, J.-B., Yi, K., Park, Y.-S., Byun, Y.-H., Joo, S., 2019. Comparative assessment of net CO2 exchange across an urbanization gradient in Korea based on eddy covariance measurements. Carbon Bal. Manag. 14, 13.
Hou, M., Hu, Y., He, Y., 2014. Modifications in vegetation cover and surface albedo during rapid urbanization: a case study from South China. Environ. Earth Sci. 72, 1659–1666.
Hu, Y., Jia, G., Pohl, C., Zhang, X., van Genderen, J., 2016. Assessing surface albedo change and its induced radiation budget under rapid urbanization with Landsat and GLASS data. Theor. Appl. Climatol. 123, 711–722.
Hu, Y., Hou, M., Zhao, C., Zhen, X., Yao, L., Xu, Y., 2019. Human-induced changes of surface albedo in Northern China from 1992-2012. Int. J. Appl. Earth Obs. Geoinf. 79, 184–191.
Huang, X., Xia, J., Xiao, R., He, T., 2019. Urban expansion patterns of 291 Chinese cities, 1990–2015. Int. J. Digit. Earth 12, 62–77.
Jacobson, M.Z., Nghiem, S.V., Sorichetta, A., Whitney, N., 2015. Ring of impact from the mega-urbanization of Beijing between 2000 and 2009. J. Geophys. Res.-Atmos. 120, 5740–5756.
Jin, M., Dickinson, R.E., Zhang, D., 2005. The footprint of urban areas on global climate as characterized by MODIS. J. Clim. 18, 1551–1565.
Jun, Z., Ronggao, L., Jiyuan, L., Guosong, Z., 2013. Radiative forcing over China due to albedo change caused by land cover change during 1990-2010. Acta Geograph. Sin. 68, 875–885.
Kalantar, B., Mansor, S., Khuzaimah, Z., Sameen, M.I., Pradhan, B., 2017. Modelling mean albedo of individual roofs in complex urban areas using satellite images and airborne laser scanning point clouds. In: International Archives of the Photogrammetry, Remote Sensing and Spatial Information Sciences - ISPRS Archives, pp. 237–240.
Kim, W., He, T., Wang, D., Cao, C., Liang, S., 2013. Assessment of long-term sensor radiometric degradation using time series analysis. IEEE Trans. Geosci. Remote Sens. 52, 2960–2976.
Kuang, W., Liu, A., Dou, Y., Li, G., Lu, D., 2019. Examining the impacts of urbanization on surface radiation using Landsat imagery. GISci. Remote Sens. 56, 462–484.
Landier, L., Lauret, N., Yin, T., Al Bitar, A., Gastellu-Etchegorry, J.P., Feigenwinter, C., Parlow, E., Mitraka, Z., Chrysoulakis, N., 2016. Remote sensing studies of urban canopies: 3D radiative transfer modeling. Sustain. Urb. 227.
Li, L., Zha, Y., 2019. Satellite-based spatiotemporal trends of canopy urban heat islands and associated drivers in China's 32 major cities. Remote Sens. 11.
Li, X., Gong, P., Liang, L., 2015. A 30-year (1984-2013) record of annual urban dynamics of Beijing City derived from Landsat data. Remote Sens. Environ. 166, 78–90.
Li, X., Zhou, Y., Asrar, G.R., Imhoff, M., Li, X., 2017. The surface urban heat island response to urban expansion: A panel analysis for the conterminous United States. Sci. Total Environ. 605-606, 426–435.
Li, X., Zhou, Y., Eom, J., Yu, S., Asrar, G.R., 2019. Projecting global urban area growth through 2100 based on historical time series data and future shared socioeconomic pathways. Earth's Future 7, 351–362.
Liang, S., 2003. A direct algorithm for estimating land surface broadband albedos from MODIS imagery. IEEE Trans. Geosci. Remote Sens. 41, 136–145.
Liang, S., Wang, D., 2017. Moderate Resolution Imaging Spectroradiometer (MODIS) Downward Shortwave Radiation (MCD18A1) and Photosynthetically Active Radiation (MCD18A2) Algorithm Theoretical Basis Document. NASA.
Liang, S.L., Strahler, A.H., Walthall, C., 1999. Retrieval of land surface albedo from satellite observations: A simulation study. J. Appl. Meteorol. 38, 712–725.
Liang, S., Stroeve, J., Box, J.E., 2005. Mapping daily snow/ice shortwave broadband albedo from Moderate Resolution Imaging Spectroradiometer (MODIS): the improved direct retrieval algorithm and validation with Greenland in situ measurement. J. Geophys. Res.-Atmos. 110.
Liang, S., Zhao, X., Liu, S., Yuan, W., Cheng, X., Xiao, Z., Zhang, X., Liu, Q., Cheng, J., Tang, H., 2013. A long-term Global Land Surface Satellite (GLASS) data-set for environmental studies. Int. J. Digit. Earth 6, 5–33.
Liu, J., Liu, M., Deng, X., Zhuang, D., Zhang, Z., Luo, D., 2002. The land use and land cover change database and its relative studies in China. J. Geogr. Sci. 12, 275–282.
Liu, J., Schaaf, C., Strahler, A., Jiao, Z., Shuai, Y., Zhang, Q., Roman, M., Augustine, J.A., Dutton, E.G., 2009. Validation of Moderate Resolution Imaging Spectroradiometer (MODIS) albedo retrieval algorithm: dependence of albedo on solar zenith angle. J. Geophys. Res.-Atmos. 114.
Liu, N., Liu, Q., Wang, L., Liang, S., Wen, J., Qu, Y., Liu, S., 2013a. A statistics-based temporal filter algorithm to map spatiotemporally continuous shortwave albedo from MODIS data. Hydrol. Earth Syst. Sci. 17, 2121–2129.
Liu, Q., Wang, L., Qu, Y., Liu, N., Liu, S., Tang, H., Liang, S., 2013b. Preliminary evaluation of the long-term GLASS albedo product. Int. J. Digit. Earth 6, 69–95.
Liu, J., Kuang, W., Zhang, Z., Xu, X., Tai, Y., Ning, J., Zhou, W., Zhang, S., Li, R., Yan, C., Wu, S., Shi, X., Jiang, N., Yu, D., Pan, X., Chi, W., 2014a. Spatiotemporal characteristics, patterns and causes of land use changes in China since the late 1980s. Acta Geograph. Sin. 69, 3–14.
Liu, Z., He, C., Zhou, Y., Wu, J., 2014b. How much of the world's land has been urbanized, really? A hierarchical framework for avoiding confusion. Landsc. Ecol. 29, 763–771.
Liu, S., Li, X., Xu, Z., Che, T., Xiao, Q., Ma, M., Liu, Q., Jin, R., Guo, J., Wang, L., Wang, W., Qi, Y., Li, H., Xu, T., Ran, Y., Hu, X., Shi, S., Zhu, Z., Tan, J., Zhang, Y., Ren, Z., 2018. The Heihe integrated observatory network: A basin-scale land surface processes observatory in China. Vadose Zone J. 17.
Liu, X., Wang, S., Wu, P., Feng, K., Hubacek, K., Li, X., Sun, L., 2019. Impacts of urban expansion on terrestrial carbon storage in China. Environ. Sci. Technol. 53, 6834–6844.
Lyu, L., Sun, F., Huang, R., 2018. Innovation-based urbanization: evidence from 270 cities at the prefecture level or above in China. Acta Geograph. Sin. 73, 1910–1922.
Mackey, C.W., Lee, X., Smith, R.B., 2012. Remotely sensing the cooling effects of city scale efforts to reduce urban heat island. Build. Environ. 49, 348–358.
Manoli, G., Fatichi, S., Schläpfer, M., Yu, K., Crowther, T.W., Meili, N., Burlando, P., Katul, G.G., Bou-Zeid, E., 2019. Magnitude of urban heat islands largely explained by climate and population. Nature 573, 55–60.
Markham, B.L., Helder, D.L., 2012. Forty-year calibrated record of earth-reflected radiance from Landsat: A review. Remote Sens. Environ. 122, 30–40.
Markham, B., Barsi, J., Kvaran, G., Ong, L., Kaita, E., Biggar, S., Czapla-Myers, J., Mishra, N., Helder, D., 2014. Landsat-8 operational land imager radiometric calibration and stability. Remote Sens. 6.
Martínez-Zarzoso, I., Maruotti, A., 2011. The impact of urbanization on CO2 emissions: evidence from developing countries. Ecol. Econ. 70, 1344–1353.
Masek, J.G., Vermote, E.F., Saleous, N.E., Wolfe, R., Hall, F.G., Huemmrich, K.F., Feng, G., Kutler, J., Teng-Kui, L., 2006. A Landsat surface reflectance dataset for North America, 1990-2000. IEEE Geosci. Remote Sens. Lett. 3, 68–72.
McCarthy, M.P., Best, M.J., Betts, R.A., 2010. Climate change in cities due to global warming and urban effects. Geophys. Res. Lett. 37.
Mohajeri, N., Gudmundsson, A., Kunckler, T., Upadhyay, G., Assouline, D., Kämpf, J.H., Scartezzini, J.L., 2019. A solar-based sustainable urban design: the effects of city-scale street-canyon geometry on solar access in Geneva, Switzerland. Appl. Energy 240, 173–190.
Morini, E., Castellani, B., De Ciantis, S., Anderini, E., Rossi, F., 2018. Planning for cooler urban canyons: comparative analysis of the influence of façades reflective properties on urban canyon thermal behavior. Sol. Energy 162, 14–27.
Qin, Y., 2015. Urban canyon albedo and its implication on the use of reflective cool pavements. Energ. Build. 96, 86–94.
Qiu, S., Zhu, Z., He, B., 2019. Fmask 4.0: improved cloud and cloud shadow detection in Landsats 4–8 and Sentinel-2 imagery. Remote Sens. Environ. 231, 111205.
Qu, Y., Liu, Q., Liang, S., Wang, L., Liu, N., Liu, S., 2014. Direct-estimation algorithm for mapping daily land-surface broadband albedo from MODIS data. IEEE Trans. Geosci. Remote Sens. 52, 907–919.
Qu, Y., Liang, S., Liu, Q., Li, X., Feng, Y., Liu, S., 2016. Estimating Arctic sea-ice shortwave albedo from MODIS data. Remote Sens. Environ. 186, 32–46.
Radwan, M.T., Blackburn, A.G., Whyatt, D.J., Atkinson, M.P., 2019. Dramatic loss of agricultural land due to urban expansion threatens food security in the Nile Delta, Egypt. Remote Sens. 11.
Reinmann, A.B., Hutyra, L.R., Trlica, A., Olofsson, P., 2016. Assessing the global warming potential of human settlement expansion in a mesic temperate landscape from 2005 to 2050. Sci. Total Environ. 545-546, 512–524.
Roy, D.P., Wulder, M.A., Loveland, T.R., Allen, R.G., Anderson, M.C., Helder, D., Irons, J. R., Johnson, D.M., Kennedy, R., Scambos, T.A., Schaaf, C.B., Schott, J.R., Sheng, Y., Vermote, E.F., Belward, A.S., Bindschadler, R., Cohen, W.B., Gao, F., Hipple, J.D., Hostert, P., Huntington, J., Justice, C.O., Kilic, A., Kovalskyy, V., Lee, Z.P., Lymburner, L., Masek, J.G., McCorkel, J., Shuai, Y., Trezza, R., Vogelmann, J.,

Wynne, R.H., Zhu, Z., 2014. Landsat-8: science and product vision for terrestrial global change research. Remote Sens. Environ. 145, 154–172.
Royer, A., Charbonneau, L., Bonn, F., 1988. Urbanization and Landsat MSS albedo change in the Windsor-Québec corridor since 1972. Int. J. Remote Sens. 9, 555–566.
Santamouris, M., Synnefa, A., Karlessi, T., 2011. Using advanced cool materials in the urban built environment to mitigate heat islands and improve thermal comfort conditions. Sol. Energy 85, 3085–3102.
Schneider, A., Mertes, C.M., 2014. Expansion and growth in Chinese cities, 1978-2010. Environ. Res. Lett. 9.
Seto, K.C., Güneralp, B., Hutyra, L.R., 2012. Global forecasts of urban expansion to 2030 and direct impacts on biodiversity and carbon pools. Proc. Natl. Acad. Sci. U. S. A. 109, 16083–16088.
Seto, K.C., Dhakal, S., Bigio, A., Blanco, H., Delgado, G.C., Dewar, D., Huang, L., Inaba, A., Kansal, A., Lwasa, S., 2014. Human settlements, infrastructure and spatial planning. In: Contribution of Working Group III to the Fifth Assessment Report of the Intergovernmental Panel on Climate Change.
Shan, Y., Guan, D., Hubacek, K., Zheng, B., Davis, S.J., Jia, L., Liu, J., Liu, Z., Fromer, N., Mi, Z., Meng, J., Deng, X., Li, Y., Lin, J., Schroeder, H., Weisz, H., Schellnhuber, H.J., 2018. City-level climate change mitigation in China. Sci. Adv. 4, eaaq0390.
Shi, D.C., Zhuang, C.Q., Lin, C.Q., Zhao, X., Chen, D.P., Gao, Y.F., Levinson, R., 2019. Effects of natural soiling and weathering on cool roof energy savings for dormitory buildings in Chinese cities with hot summers. In: Solar Energy Materials and Solar Cells, p. 200.
Shindell, D., Myhre, G., Boucher, O., Forster, P., Breon, F.-M., Fuglestvedt, J., 2013. Radiative forcing in the ar5. In: Conference Proceeding in IPCC AR5 Working Group I, pp. 1–11.
Shuai, Y., Masek, J.G., Gao, F., Schaaf, C.B., 2011. An algorithm for the retrieval of 30-m snow-free albedo from Landsat surface reflectance and MODIS BRDF. Remote Sens. Environ. 115, 2204–2216.
Shuai, Y., Masek, J.G., Gao, F., Schaaf, C.B., He, T., 2014. An approach for the long-term 30-m land surface snow-free albedo retrieval from historic Landsat surface reflectance and MODIS-based a priori anisotropy knowledge. Remote Sens. Environ. 152, 467–479.
Sugawara, H., Takamura, T., 2014. Surface albedo in cities: case study in Sapporo and Tokyo, Japan. Bound.-Layer Meteorol. 153, 539–553.
Tang, R., Zhao, X., Zhou, T., Jiang, B., Wu, D., Tang, B., 2018. Assessing the impacts of urbanization on albedo in Jing-Jin-Ji region of China. Remote Sens. 10, 1096.
Trlica, A., Hutyra, L.R., Schaaf, C.L., Erb, A., Wang, J.A., 2017. Albedo, land cover, and daytime surface temperature variation across an urbanized landscape. Earth's Future 5, 1084–1101.
Vahmani, P., Sun, F., Hall, A., Ban-Weiss, G., 2016. Investigating the climate impacts of urbanization and the potential for cool roofs to counter future climate change in Southern California. Environ. Res. Lett. 11, 124027.
Vermote, E.F., Tanre, D., Deuze, J.L., Herman, M., Morcette, J., 1997. Second simulation of the satellite signal in the solar Spectrum, 6S: an overview. IEEE Trans. Geosci. Remote Sens. 35, 675–686.
Vermote, E., Justice, C., Claverie, M., Franch, B., 2016. Preliminary analysis of the performance of the Landsat 8/OLI land surface reflectance product. Remote Sens. Environ. 185, 46–56.
Wang, Z., Barlage, M., Zeng, X., Dickinson, R.E., Schaaf, C.B., 2005. The solar zenith angle dependence of desert albedo. Geophys. Res. Lett. 32.
Wang, G., Jiang, W., Wei, M., Xu, J., 2006. Analysis for urban/rural albedo from MODIS over East China. In: Remote Sensing and Space Technology for Multidisciplinary Research and Applications. International Society for Optics and Photonics, p. 61990F.
Wang, X., Piao, S., Ciais, P., Li, J., Friedlingstein, P., Koven, C., Chen, A., 2011. Spring temperature change and its implication in the change of vegetation growth in North America from 1982 to 2006. Proc. Natl. Acad. Sci. 108, 1240.
Wang, D., Liang, S., He, T., Yu, Y., 2013. Direct estimation of land surface albedo from VIIRS data: algorithm improvement and preliminary validation. J. Geophys. Res.-Atmos. 118, 12,577-512,586.
Wang, D., Liang, S., He, T., Yu, Y., Schaaf, C., Wang, Z., 2015. Estimating daily mean land surface albedo from MODIS data. J. Geophys. Res.-Atmos. 120, 4825–4841.
Wang, Z., Erb, A.M., Schaaf, C.B., Sun, Q., Liu, Y., Yang, Y., Shuai, Y., Casey, K.A., Román, M.O., 2016. Early spring post-fire snow albedo dynamics in high latitude boreal forests using Landsat-8 OLI data. Remote Sens. Environ. 185, 71–83.
Wang, Z., Schaaf, C.B., Sun, Q., Kim, J., Erb, A.M., Gao, F., Román, M.O., Yang, Y., Petroy, S., Taylor, J.R., Masek, J.G., Morisette, J.T., Zhang, X., Papuga, S.A., 2017. Monitoring land surface albedo and vegetation dynamics using high spatial and temporal resolution synthetic time series from Landsat and the MODIS BRDF/NBAR/albedo product. Int. J. Appl. Earth Obs. Geoinf. 59, 104–117.
Wang, D., Liang, S., Zhang, Y., Gao, X., Brown, M.G.L., Jia, A., 2020. A new set of MODIS land products (MCD18): downward shortwave radiation and photosynthetically active radiation. Remote Sens. 12.
Woodcock, C.E., Loveland, T.R., Herold, M., Bauer, M.E., 2020. Transitioning from change detection to monitoring with remote sensing: A paradigm shift. Remote Sens. Environ. 238, 111558.
Xu, X., Liu, J., Zhuang, D., 2012. Remote sensing monitoring methods of land use /cover change in national scale. J. Anhui Agric. Sci. 40, 2365–2369.
Xu, X., AzariJafari, H., Gregory, J., Norford, L., Kirchain, R., 2020. An integrated model for quantifying the impacts of pavement albedo and urban morphology on building energy demand. Energ. Build. 211, 109759.
Yang, X., Li, Y., 2015. The impact of building density and building height heterogeneity on average urban albedo and street surface temperature. Build. Environ. 90, 146–156.
Yang, F., Mitchell, K., Hou, Y.-T., Dai, Y., Zeng, X., Wang, Z., Liang, X.-Z., 2008. Dependence of land surface albedo on solar zenith angle: observations and model parameterization. J. Appl. Meteorol. Climatol. 47, 2963–2982.
Yao, R., Wang, L., Huang, X., Niu, Z., Liu, F., Wang, Q., 2017. Temporal trends of surface urban heat islands and associated determinants in major Chinese cities. Sci. Total Environ. 609, 742–754.
Zhang, Y., Liang, S., 2018. Impacts of land cover transitions on surface temperature in China based on satellite observations. Environ. Res. Lett. 13.
Zhang, H., Roy, D.P., 2016. Landsat 5 thematic mapper reflectance and NDVI 27-year time series inconsistencies due to satellite orbit change. Remote Sens. Environ. 186, 217–233.
Zhao, L., Lee, X., Smith, R.B., Oleson, K., 2014. Strong contributions of local background climate to urban heat islands. Nature 511, 216.
Zhou, D., Zhao, S., Liu, S., Zhang, L., Zhu, C., 2014. Surface urban heat island in China's 32 major cities: spatial patterns and drivers. Remote Sens. Environ. 152, 51–61.
Zhou, D., Xiao, J., Bonafoni, S., Berger, C., Deilami, K., Zhou, Y., Frolking, S., Yao, R., Qiao, Z., Sobrino, A.J., 2018a. Satellite remote sensing of surface urban heat islands: Progress, challenges, and perspectives. Remote Sens. 11.
Zhou, Y., Li, X., Asrar, G.R., Smith, S.J., Imhoff, M., 2018b. A global record of annual urban dynamics (1992–2013) from nighttime lights. Remote Sens. Environ. 219, 206–220.
Zoran, M.A., Dida, A.I., Zoran, L.F., 2018. Impact of extreme climate events and anthropogenic stressors on urban green albedo assessed from time-series MODIS satellite data. In: Earth Resources and Environmental Remote Sensing/GIS Applications IX. International Society for Optics and Photonics, p. 107901T.